Analysis of sheet metal formability through isotropic and kinematic hardening models

Marilena C. Butuc, Cristian Teodosiu, Frédéric Barlat, José J. Gracio

Title: Analysis of sheet metal formability through isotropic and kinematic hardening models

Authors: Marilena C. Butuc, Cristian Teodosiu, Frédéric Barlat, José J. Gracio

PII: S0997-7538(11)00039-8

DOI: 10.1016/j.euromechsol.2011.03.005

Reference: EJMSOL 2691

To appear in: *European Journal of Mechanics / A Solids*

Received Date: 24 November 2010

Revised Date: 14 March 2011

Accepted Date: 15 March 2011

Please cite this article as: Butuc, M.C., Teodosiu, C., Barlat, F., Gracio, J. Analysis of sheet metal formability through isotropic and kinematic hardening models, European Journal of Mechanics / A Solids (2011), doi: 10.1016/j.euromechsol.2011.03.005

Analysis of sheet metal formability through isotropic and kinematic hardening models

Marilena C. Butuc[a,1], Cristian Teodosiu[b], Frédéric Barlat[a, c], José J. Gracio[a]

[a] Centro de Tecnologia Mecânica e Automação, Universidade de Aveiro, Campus Universitário de Santiago, 3810-193 Aveiro, Portugal

[b] The Institute of Physical and Chemical Research (RIKEN), 2-1 Hirosawa, Wako-shi, Saitama, 351-0198 Japan

[c] Materials Mechanics Laboratory (MML), Graduate Institute of Ferrous Technology (GIFT), Pohang University of Science and Technology (POSTECH), San 31 Hyoja-dong, Nam-gu, Pohang, Gyeongbuk 790-784, Republic of Korea

Abstract

The present paper aims at analysing the sheet metal formability through several isotropic and kinematic hardening models. Specifically, a special attention is paid to the physically-based hardening model of Teodosiu and Hu (1995), which accounts for the anisotropic work-hardening induced by the microstructural evolution at large strains, as well as to some more conventional hardening models, including the isotropic Swift strain–hardening power law, and the Voce saturation strain-hardening law, combined with a non-linear kinematic hardening described by the Armstrong-Frederick law. The onset of localized necking is simulated by an advanced sheet metal forming limit model which connects, through the Marciniak-Kuczinsky analysis, the hardening models with the anisotropic yield criterion Yld2000-2d (Barlat et al., 2003). Both linear and complex strain paths are taken into account. The selected material is a DC06 steel sheet. The validity of each model is assessed by comparing the predicted forming limits with experimental results carefully obtained on this steel. The origin of discrepancy in the predicted results using different hardening models is thoroughly analyzed.

Keywords: Constitutive laws; Anisotropic; Hardening; Kinematic; Limit analysis; Numerical methods

[1] Corresponding author. Tel.: +351 234 370830; Fax: +351 234 370953
E-mail: cbutuc@ua.pt

1. Introduction

The formability issue could be monitored by a good understanding of the deformation processes, of the plastic flow, and of the factors limiting the forming of metal sheets. The Forming Limit Diagram (FLD), introduced by Keeler (1965) and Goodwin (1968), is still the most frequently applied method in industry to predict the formability of sheet metals. It is well known that the forming limits are influenced by several physical factors of which the most important ones are the material work-hardening, the strain rate sensitivity, the plastic anisotropy, the development of structural damage and, last but not least, the strain path. However, it is difficult to experimentally assess the influence of each parameter individually, since it is virtually impossible to change only one at a time. Moreover, the experimental determination of the forming limits in all sheet metal forming processes is tedious, expensive and hardly possible, since the strain paths of material points are generally non-linear and differ from each other.

On the other hand, the theoretical analysis of plastic instability and flow localization may supply relevant information to prevent the failure of the sheet metal forming process, to examine the influence of each parameter on the necking occurrence, and to improve the press performance. Therefore, an extensive effort has been devoted to the development of mathematical models capable of accurately predicting the plastic flow localization in the course of sheet metal forming processes. To date, the Marciniak-Kuczinsky (MK) (1967) analysis, which supposes an infinite sheet metal containing a region of local imperfection where heterogeneous plastic flow develops and localizes, has become one of the most important tools in predicting the sheet metal formability. The predicted limit strains strongly depend on the constitutive law incorporated in the MK analysis. Appropriate constitutive models able to describe analytically the plastic behaviour of orthotropic metals allow a better prediction of limit strains. Hence, the combination of the MK analysis with advanced constitutive models is a fruitful device in understanding the material behaviour and predicting the necking occurrence (see e.g. Butuc, 2004).

Industrial complex parts are manufactured by multi-stage forming operations. The strain-path evolution is generally quite complex and may include sharp changes inducing a dramatic reduction in the formability. For larger strains and for such severe strain-path changes, the evolution of the strain hardening is an issue and has been the subject of an intensive research. Tvergaard (1978) investigated the localized necking for

elastic-plastic sheets under biaxial stretching localized necking, assuming that the material follows a kinematic hardening rule of Ziegler type. He found that a kinematic hardening model accelerates the strain localization in the same way as the corner models, although to a lower extent. He also concluded that the forming limit curves predicted by kinematic hardening are in far better agreement with experimental results than the similar curves predicted by standard flow theory with isotropic hardening, especially for high-hardening materials, for which a considerable translation of the yield surface occurs in stress space. Using the MK analysis to compare the effect of a combined isotropic and kinematic hardening on the FLDs, Lu and Lee (1987) found that the kinematic hardening model predicted forming limits closer to experimental data for steel sheets under proportional loading. On the other hand, the isotropic hardening model gives better predictions of the forming limits with uniaxial prestrain followed by equibiaxial straining. Hiwatashi *et al.* (1998) studied the effect of strain path for proportional and two-stage straining on the FLDs of a mild steel, through the use of the MK analysis, and combining a model of texture anisotropy (Van Houtte *et al.*, 1995) with the microstructure-based anisotropic hardening model of Teodosiu and Hu (1995). It was shown that the forming limit for the case of two-stage straining depends on the amount of the first straining and the combination of first and second strain-path modes. Yao and Cao (2002) proposed a methodology to determine the evolution of yield surface in a large plastic deformation process. This evolution is expressed in terms of changes in back stress and yield surface curvature, which are assumed to be proportional to the accumulated plastic strain. Using this approach they found a great improvement of the predicted FLDs under various loading conditions for Al2008 and Al6111. Hashiguchi and Protasov (2004) analysed the localized necking by the so-called sub-loading surface model, which is applicable to an arbitrary loading behaviour of elastoplastic materials with an arbitrary yield surface. They concluded that not only the tangential-strain rate but also the inherent/induced anisotropy due to the kinematic hardening intensely influences the onset of localized necking. Unlike the previously cited authors, Stoughton and Zhu (2004) remarked that, although kinematic effects are critical with respect to springback, it is not clear whether they play a significant role in most path-dependent FLC data, such as those reported by Graf and Hosford (1993) for Al2008-T4. They argued that by the very transient nature of kinematic effects, stresses tend to rapidly rise to the level expected under isotropic hardening after a few percent additional strains along a new path. Concerning this remark it should be noticed,

however, that a permanent softening may occur, as has been frequently observed in various materials under reverse loading, in particular for the DC06 steel analyzed in this paper. Therefore, stresses would not necessary reach after reversal the level expected under isotropic hardening (or monotonic loading).

Signorelli *et al.* (2009) analyzed forming-limit strains of metals using a rate-dependent plasticity, polycrystalline, self-consistent model, in conjunction with the MK approach. They found that the calculation of the FLD with a more realistic scale transition successfully predicts some of the experimental tendencies that the Taylor model cannot reproduce for aluminium alloys Al6116-T4 and Al5182-O. Moreover, they concluded that future improvements of the current model would include a more accurate description of the microstructural evolution, which can be taken into account through dislocation-strain, work-hardening based models.

The above review of some of the pertinent literature shows that, although the influence of the hardening evolution on the FLDs has been considered and continues to be treated by several authors, there is still a need to systematically analyze the correlation between the hardening models and predicted forming limits, by using reliable experimental data both for the mechanical behaviour and the FLDs, under linear and complex strain-paths.

The present paper aims at fulfilling this requirement, by using as reference material the DC06 steel sheet. The microstructural model of Teodosiu and Hu (1995) proved to be able to predict with a very good accuracy the strain-induced anisotropy of this material, such as the Bauschinger effect, the cross and transient hardening, up to large plastic strains (see also Bouvier *et al.*, 2006a, 2006b; Haddadi *et al.*, 2006). Therefore, in the present work this microstructural model, as well as various combinations of more classical models of isotropic and non-linear kinematic hardening will be used to describe the anisotropic hardening behaviour of a DC06 steel sheet. The yield locus is described by the Yld2000-2d yield function (Barlat *et al.*, 2003). The forming limits are computed using an advanced model for predicting the FLDs under linear and complex loadings developed on the base of the MK analysis.

The originality of this contribution consists in (*i*) the use of several isotropic and non-linear kinematic hardening models that have been identified for DC06 steel sheet on the

base of a comprehensive set of experimental tests, including the microstructural hardening model specially developed for this kind of material; (ii) the comparison of the predicted forming limits with trustworthy experimental data, and (iii) the analysis of the effect of kinematic hardening on the occurrence of plastic flow localization. A particular attention will be also paid to the formability under strain-path changes involving biaxial prestrain followed by uniaxial tension and the reverse sequence.

The paper is organized as follows. Section 2 presents briefly the selected constitutive equations, namely the anisotropic hardening model of Teodosiu and Hu (1995), insisting on the microstructural significance of the internal state variables and on their evolution equations, as well as some more conventional hardening models, and on the plane-stress, anisotropic yield function Yld2000-2d. Section 3 summarizes the use of the MK-model in conjunction with the adopted constitutive equations for calculating the FLDs under plane stress conditions. Section 4 begins by the presentation of the complete set of material parameters involved in the adopted models for DC06 steel. Then, experimental FLDs obtained when subjecting this material to linear and complex strain paths are compared with the theoretical estimates obtained by using the MK model. The remaining part of this section is devoted to an analysis of the predicted forming limits, as well as to the significance of the back stress on the formability of metal sheets. The paper ends with a brief summary and conclusions.

2. Review of the selected constitutive equations

In this paper, vector and tensor variables are denoted by bold-face symbols. If **A** and **B** are second-order tensors and **C** is a fourth-order tensor, the double-contracted tensor products between such tensors are defined in terms of their Cartesian components as

$$\boldsymbol{A} : \boldsymbol{B} = A_{ij} B_{ij,} \tag{1}$$

$$\boldsymbol{A} : \boldsymbol{C} : \boldsymbol{B} = A_{ij} C_{ijkl} B_{kl.} \tag{2}$$

The norm of a second-order tensor $\boldsymbol{A}$ is defined as the square root of the double-contracted tensor product of such tensor by itself, i.e.

$$\left|\boldsymbol{A}\right| = \sqrt{\boldsymbol{A} : \boldsymbol{A}}. \tag{3}$$

2.1 Hardening models

2.1.1 Phenomenological hardening models

In the present work four classical hardening models are selected. We give here a brief description of their evolution equations and the acronyms that will be used for these models in the presentation of the numerical results.

Isotropic hardening models

1. The Swift law (acronym Swift) expresses the strain hardening by the power law

$$\sigma_{\mathrm{Y}} = C_{\mathrm{R}} \left(\varepsilon_0 + \bar{\varepsilon} \right)^n , \tag{4}$$

where σ_{Y} is the yield stress, $\bar{\varepsilon}$ the effective plastic strain, while C_{R}, ε_0 and n are material parameters.

2. The Voce law (acronym Voce) expresses the strain hardening by the saturation law

$$\sigma_{\mathrm{Y}} = Y_0 + R , \tag{5}$$

$$\dot{R} = C_{\mathrm{R}} \left(R_{\mathrm{sat}} - R \right) \dot{\bar{\varepsilon}}, \qquad R(0) = 0, \tag{6}$$

where σ_{Y} is the yield stress, $\bar{\varepsilon}$ the effective strain, while Y_0, C_{R} and R_{sat} are material constant parameters

Anisotropic hardening models

1. The first anisotropic hardening model (acronym Swift + KH) uses the Swift power law to describe the isotropic hardening combined with the Armstrong-Frederick law to describe the kinematic hardening. The evolution equations are

$$\sigma_{\mathrm{Y}} = C_{\mathrm{R}} \left(\varepsilon_0 + \bar{\varepsilon} \right)^n , \tag{7}$$

$$\dot{\boldsymbol{X}} = C_{\mathrm{X}} \left(\frac{X_{\mathrm{sat}}}{\bar{\sigma}_e} \left(\boldsymbol{\sigma}' - \boldsymbol{X} \right) - \boldsymbol{X} \right) \dot{\bar{\varepsilon}}, \quad \boldsymbol{X}(0) = \mathbf{0}, \tag{8}$$

where C_{R}, C_{X}, X_{sat}, ε_0 and n are material parameters.

2. The second anisotropic hardening model (acronym Voce + KH) uses the Voce saturation law to describe the isotropic hardening, combined with the Armstrong-Frederick law to describe the kinematic hardening. The evolution equations are

$$\sigma_{\mathrm{Y}} = Y_0 + R, \tag{9}$$

$$\dot{R} = C_{\mathrm{R}} \left(R_{\mathrm{sat}} - R \right) \dot{\bar{\varepsilon}}, \qquad R(0) = 0, \tag{10}$$

$$\dot{\boldsymbol{X}} = C_{\mathrm{X}}\left(\frac{X_{\mathrm{sat}}}{\bar{\sigma}_e}\left(\boldsymbol{\sigma}' - \boldsymbol{X}\right) - \boldsymbol{X}\right)\dot{\bar{\varepsilon}}, \quad \boldsymbol{X}(0) = \boldsymbol{0}, \tag{11}$$

where Y_0, C_{R}, R_{sat}, $\mathrm{C_X}$ and X_{sat} are material parameters.

2.1.2 Microstructural hardening model

The microstructural hardening model of Teodosiu and Hu (1995) (acronym MicMod) and its subsequent evolution is described in detail e.g. by Haddadi *et al.* (2006). For ease of reference, a brief review of the model is presented in the following. Based on the microstructural evidence and on the fact that the plastic behaviour of metals depends not only on the current state of deformation, but also on the deformation history, this model describes the hardening of the material by four internal state variables, denoted by {R, $\boldsymbol{X}$, $\boldsymbol{S}$, $\boldsymbol{P}$}. R, $\boldsymbol{S}$ and $\boldsymbol{X}$ have the dimension of stress, $\boldsymbol{P}$ has no dimension. R is a scalar, $\boldsymbol{S}$ is a fourth-order tensor, and $\boldsymbol{P}$ and $\boldsymbol{X}$ are second-order tensors. For a well-annealed material, the initial values of all these variables are zero. The evolution laws of the internal state variables are written in a work-hardening/recovery format, reflecting the dynamic processes of the production/annihilation of dislocations and of the formation/dissolution of planar dislocation structures.

The evolution of R is given by

$$\dot{R} = C_{\mathrm{R}}\left(R_{\mathrm{sat}} - R\right)\dot{\bar{\varepsilon}}, \qquad R(0) = 0, \tag{12}$$

where C_{R} characterizes the rate of the isotropic hardening produced by randomly accumulated dislocations, R_{sat} is the saturation value of R, and $\dot{\bar{\varepsilon}}$ is the power-equivalent plastic strain rate.

The evolution of the tensor $\boldsymbol{P}$, which describes the polarity of planar dislocation structures, is given by

$$\dot{\boldsymbol{P}} = C_{\mathrm{P}}\left(\boldsymbol{A} - \boldsymbol{P}\right)\dot{\bar{\varepsilon}}, \qquad \boldsymbol{P}(0) = \boldsymbol{0}, \tag{13}$$

where $\boldsymbol{A}$ is the current direction of the plastic strain rate tensor, and C_{P} characterizes the rate at which the polarity tensor $\boldsymbol{P}$ tends to $\boldsymbol{A}$.

The deviatoric tensor variable $\boldsymbol{X}$, called the back stress, is intended to describe the rapid changes in stress under strain-path changes. The evolution of $\boldsymbol{X}$ is governed by the equation

$$\dot{\boldsymbol{X}} = C_{\mathrm{X}}\left(\frac{X_{\mathrm{sat}}}{\bar{\sigma}_e}(\boldsymbol{\sigma}' - \boldsymbol{X}) - \boldsymbol{X}\right)\dot{\bar{\varepsilon}}, \qquad \boldsymbol{X}(0) = \mathbf{0}, \tag{14}$$

where C_{X} characterizes the saturation rate of $\boldsymbol{X}$, X_{sat} is a material parameter characterizing the saturation value of the norm $|\boldsymbol{X}|$ of the back stress, $\boldsymbol{\sigma}'$ is the deviator of the Cauchy stress tensor, and $\bar{\sigma}_e$ is the equivalent stress corresponding to the effective stress tensor $\boldsymbol{\sigma}' - \boldsymbol{X}$. The dependence of $\boldsymbol{X}$ on the persistent dislocation structures is described by the scalar function $X_{\mathrm{sat}}(\boldsymbol{S}, \boldsymbol{A})$. Specifically, it is assumed that

$$X_{\mathrm{sat}} = X_0 + (1-m)\sqrt{S_{\mathrm{D}}^2 + q|\boldsymbol{S}_{\mathrm{L}}|^2}, \tag{15}$$

where X_0 is the initial value of X_{sat}, q and m are material parameters, while S_{D} and $\boldsymbol{S}_{\mathrm{L}}$ are defined by the decomposition given in Eq. (8) below.

The tensor variable **S**, which describes the directional strength of planar dislocation structures is the most important descriptor of the microstructure organization in this hardening model. It may be decomposed as

$$\boldsymbol{S} = S_{\mathrm{D}}\boldsymbol{A} \otimes \boldsymbol{A} + \boldsymbol{S}_{\mathrm{L}}, \tag{16}$$

with $S_{\mathrm{D}} = \boldsymbol{A} : \boldsymbol{S} : \boldsymbol{A}$. S_{D} is related to the currently active slip systems, hence to $\boldsymbol{A}$, and $\boldsymbol{S}_{\mathrm{L}}$ to the latent part of the dislocation structures.

The evolution of S_{D} is governed by the equation

$$\dot{S}_{\mathrm{D}} = C_{\mathrm{SD}}\left[h_{\mathrm{P}}(S_{\mathrm{sat}} - S_{\mathrm{D}}) - h_{\mathrm{X}}\, S_{\mathrm{D}}\right]\dot{\bar{\varepsilon}}, \tag{17}$$

where C_{SD} and S_{sat} are material parameters. The slight variation of S_{D} at the beginning of the reversed deformation in a Bauschinger test is described by the scalar function

$$h_{\boldsymbol{X}} = \frac{1}{2}\left(1 - \frac{\boldsymbol{X} : \boldsymbol{A}}{X_{\mathrm{sat}}(\boldsymbol{\sigma}' - \boldsymbol{X}) : \boldsymbol{A}}\bar{\sigma}_e\right). \tag{18}$$

The occurrence of work-hardening stagnation followed by the resumption of work-hardening, which has been observed experimentally for some severely prestrained materials under subsequent reversed deformations, is described by the function

$$\mathrm{h}_P = \begin{cases} 1 - \dfrac{C_{\mathrm{P}}}{C_{\mathrm{SD}} + C_{\mathrm{P}}} \left| \dfrac{S_{\mathrm{D}}}{S_{\mathrm{sat}}} - \boldsymbol{P} : \boldsymbol{A} \right|, & \text{if } \boldsymbol{P} : \boldsymbol{A} \geq 0, \\ \left(1 + \boldsymbol{P} : \boldsymbol{A}\right)^{n_{\mathrm{P}}} \left(1 - \dfrac{C_{\mathrm{P}}}{C_{\mathrm{SD}} + C_{\mathrm{P}}} \dfrac{S_{\mathrm{D}}}{S_{\mathrm{sat}}} \right), & \text{otherwise.} \end{cases} \tag{19}$$

The evolution of $\boldsymbol{S}_{\mathrm{L}}$ results from the interaction between microbands generated by newly activated slip planes after a strain-path change and the preformed dislocation walls. Hence, the evolution equation for the tensor $\boldsymbol{S}_{\mathrm{L}}$ takes into account the fact that the strength of the latent dislocation structures may decrease with progressing deformation, due to the disorganizing action of the cutting microbands:

$$\dot{\boldsymbol{S}}_{\mathrm{L}} = -C_{\mathrm{SL}} \left(\frac{\left| \boldsymbol{S}_{\mathrm{L}} \right|}{S_{\mathrm{sat}}} \right)^{n_{\mathrm{L}}} \boldsymbol{S}_{\mathrm{L}} \, \dot{\bar{\varepsilon}}, \tag{20}$$

where C_{SL} characterizes the rate of disorganization of the preformed dislocation structures, and n_{L} is a material parameter

The yield stress is given by

$$\sigma_{\mathrm{Y}} = Y_0 + R + mS, \tag{21}$$

where Y_0 is the initial yield stress, m is a material parameter and S is the norm of $\boldsymbol{S}$, i.e.

$$S = \left| \boldsymbol{S} \right| = \sqrt{| \boldsymbol{S}_{\mathrm{L}} |^2 + S_{\mathrm{D}}^2}. \tag{22}$$

The model involves 13 material parameters, namely Y_0, X_0, S_{sat}, R_{sat}, C_{P}, C_{SL}, C_{SD}, C_{X}, C_{R}, n_{P}, n_{L}, m and q.

2.2 The Yld2000-2d yield function

The Yld2000-2d plane stress yield function introduces the plastic anisotropy by using two linear transformations on the Cauchy stress tensor (Barlat *et al.*, 2003). It is expressed in terms of the deviatoric stress components (Barlat *et al.*, 2007) as

$$\phi = \phi'\left(\tilde{\boldsymbol{S}}'\right) + \phi''\left(\tilde{\boldsymbol{S}}''\right) = 2\bar{\sigma}_{\mathrm{Y}}^{a}, \tag{23}$$

where ϕ' and ϕ'' are two isotropic functions defined by

$$\phi'\left(\tilde{\boldsymbol{S}}'\right) = \left| \tilde{S}'_1 - \tilde{S}'_2 \right|^a, \tag{24}$$

$$\phi''\left(\tilde{\boldsymbol{S}}''\right) = \left|2\tilde{S}_2'' + \tilde{S}_1''\right|^a + \left|2\tilde{S}_1'' + \tilde{S}_2''\right|^a, \tag{25}$$

while $\tilde{\boldsymbol{S}}'$ and $\tilde{\boldsymbol{S}}''$ are linear transformations of the effective stress tensor $\boldsymbol{s}$, which is defined as difference between the deviatoric part $\boldsymbol{\sigma}'$ of the Cauchy stress and the back stress $\boldsymbol{X}$, i.e.

$$\boldsymbol{s} = \boldsymbol{\sigma}' - \boldsymbol{X}. \tag{26}$$

Hence

$$\tilde{\boldsymbol{S}}' = \boldsymbol{C}'\boldsymbol{s}, \qquad \tilde{\boldsymbol{S}}'' = \boldsymbol{C}''\boldsymbol{s}, \tag{27}$$

where $\boldsymbol{C}'$ and $\boldsymbol{C}''$ represent the linear transformations of the effective stress tensor **s** and contain the material anisotropy coefficients, which are computed using as input the experimental values of the stresses and anisotropy factors in tension along three directions and the balanced biaxial flow stress as well as the balanced biaxial anisotropy coefficient.

3. Theoretical computation of the Forming Limit Diagram

The simulation of plastic instability is carried out by using a MK-type analysis, schematically illustrated in Figure 1. This section summarizes the main steps of the theoretical computation (for details see the Appendix). The model is based on the growth by plastic deformation within a thin sheet of an initial defect in the form of a groove-like, narrow band of diminished thickness. A plane stress condition is assumed throughout. The initial inclination angle of the band with respect to the minor principal axis of the stress tensor is denoted by ψ_0. The initial value of the geometrical defect is characterized by the ratio e_0^b / e_0^a where e_0^a and e_0^b are the initial thickness in the homogeneous region and in the groove respectively. The *x, y, z*-axes correspond to rolling, transverse and normal directions of the sheet, whereas *1* and *2* represent the principal stress and strain directions in the homogeneous region. The set of axes bound to the groove is represented by *n, t, z*, where *t* denotes the longitudinal axis.

It is supposed that the material has a rigid-plastic, rate-independent behaviour. Several isotropic and anisotropic hardening models are considered to describe the hardening behaviour of material. The initial shape of the yield locus is given by the Yld2000-2d plane stress yield function (Barlat et al., 2003).

Small increments of equivalent strain are imposed in the homogeneous region, the corresponding stress and strain states being computed according to the selected constitutive equations. In order to define the strain and stress states within the band, the Newton-Raphson method is applied for solving a system of two polynomial functions resulting from the yield criterion and the requirement of deformation compatibility in the longitudinal direction of the necking band. The Jacobian matrix required in the Newton-Raphson computation is based on an analytical differentiation of the constitutive equations of the model. When the effective strain increment in the band ($d\bar{\varepsilon}^b$) becomes 10 times larger[2] than the one in the homogeneous zone ($d\bar{\varepsilon}^a$), it is considered that a plastic flow localization occurs in the band, whereas the corresponding accumulated principal strains in the homogeneous zone define the forming strain limits. For each considered strain path, the analysis is repeated for different values of ψ_0 (between 0 and 90 degrees) and the limit point on the FLD is obtained through the minimization of the principal strain ε_{11}^a in the homogeneous zone versus ψ_0.

The simulation of the complex strain paths involves a prestrain of the homogeneous zone followed by a more or less sharp change in strain path. Specifically, the sheet metal is unloaded to a zero-stress state after the prestrain and subsequently reloaded following the second strain path. To account for complex strain paths at large plastic strains, the prestrain will be accounted for when considering the evolution of the internal variables of the microstructural hardening model. More precisely, the initial values of the internal variables at the beginning of the second loading are taken equal to their values at the end of the first loading. In addition, it is also considered that the initial band orientation at the beginning of the second strain path is the one achieved at the end of the first deformation stage.

4. Results and discussion

For the validation of the simulated FLDs, the experimental FLDs carried out by DEMEGI – Engineering Faculty of the University of Porto, Portugal, presented in (Butuc, 2004) are used. The identification of the hardening models was performed by

[2] The choice of this conventional threshold is practically irrelevant for the computed FLDs, as the strain-rate in the groove increases very rapidly after this condition is attained, because of the low current hardening rate. Supplementary numerical tests carried out with the MicMod model, by using a threshold varying from 5 to 1000, have confirmed this conjecture, the corresponding FLD diagrams being practically indistinguishable.

Laboratory of the Mechanical and Thermodynamic Properties of Materials (LPMTM), University Paris 13, France, in the framework of the international research program Digital Die Design System (3DS Report, 2001).

4.1 Materials characterization

The selected material is a DC06 steel sheet, which is an aluminium-killed and titanium-treated mild steel, which is presently considered as the reference metal for the "body in white" in the automotive industry. Table 1 presents the corresponding values of the yield stresses, ultimate tensile strengths, maximum uniform elongations and anisotropy factor *r*, for three orientations of the uniaxial tensile direction with respect to the rolling direction.

The balanced biaxial yield stress σ_b was identified by means of a polycrystalline model, while the anisotropy coefficient r_b was calculated from the Yld96 yield function (Barlat et al., 1997). Their values are presented in Table 2.

Table 3 shows the values of the eight parameters $(\alpha_1,\alpha_2,\alpha_3,\alpha_4,\alpha_5,\alpha_6,\alpha_7,\alpha_8)$ of the Yld00-2d yield function, as obtained by a numerical identification from the experimental data $(\sigma_0,\sigma_{45},\sigma_{90},\sigma_b,r_0,r_{45},r_{90},r_b)$.

The selected five hardening models were identified and validated on the same very extensive ensemble of tests, including, tensile tests at various orientations with respect to the rolling direction, simple shear tests up to 80% amount of shear, and various strain-path changes, like Bauschinger tests after different amounts (10%, 20% and 30%) of forward shear strains, on specimens oriented along the rolling direction, orthogonal strain-path changes. Bilinear strain-path changes have been mainly realized by sequences of simple shear and/or uniaxial tension on smaller specimens cut out from the homogeneously deformed parts of larger predeformed specimens. All tests have been conducted by using very precise, optical measurement of the local strains on fiducial grids, and the cutting of the specimens has been done by electro-erosion, in order to avoid any damage or supplementary hardening of the specimens. The techniques used to carry out the experiments and to identify and validate the constitutive models have been

described in detail in several papers (see e.g. Haddadi *et al.*, 2006, and the references herein).

Tables 4, 5 and 6 contain the material parameters of the DC06 steel sheet involved in the hardening models MicMod, Swift and Swift+KH, Voce and Voce+KH, respectively. Figures 2a, 2b and 2c show the values of the parameters obtained by identification of the MicMod, Swift+KH and Voce+KH models, according to the 3DS Report (2001). It is observed that the microstructural model fits very accurately the experimental data for all selected tests, including the strain-hardening stagnation in large-deformation Bauschinger tests and of the softening occurring after orthogonal strain-path changes. This excellent predicting performance of the model under linear and complex strain-path changes loading is obviously due to its supplementary, physically-based internal state variables. The more conventional models Swift+KH and Voce+KH are also able to adequately fit the general level of stress, but localized phenomena such as the work-hardening stagnation or softening, which may be quite relevant for plastic localization, are not predicted correctly.

Fig. 2d shows the experimental true stress-true strain curve for DC06 steel sheet under uniaxial tension until the plastic instability occurrence and the computed ones using various hardening models like the microstructural hardening model, Swift law, Swift law + kinematic hardening expressed by the Armstrong and Frederick law, Voce law and Voce law + kinematic hardening expressed by the Armstrong and Frederick law. A rather good approximation is observed for all used models within this strain range. However, some finer, but relevant details of the ability of the compared models to fit the experimental results may be noticed even in the case of the basic uniaxial tensile test. Indeed, all models describe quite well the experimental tensile stress-strain curve as concerns the ordinates of the diagrams. On the other hand, noticeable differences between the models occur in the variation of the slopes and of the curvatures of the diagrams, which play a significant role in the prediction of the strain localization. Clearly, the model MicMod is able to better fit not only the transient variations in the hardening rate following the strain-path changes, but also the monotonous stress-strain curves, because the supplementary internal state variables correspond to different hardening mechanisms that are dominant at small, medium and large strains, thus determining the complex evolution of the rate-hardening.

The anisotropic yield criterion Yld2000-2d proved to characterize very well the initial plastic anisotropy of the studied DC06 steel sheet, as expressed by the yield stresses and r-values. Indeed, as shown in Table 7, the predicted normalized yield stresses and anisotropy factors reproduce perfectly well the experimental values. Therefore, the Yld2000-2d yield function will be adopted throughout this paper, when comparing the FLD predictions obtained by various hardening models, without further mentioning of this choice.

4.2 Forming Limit Diagrams: Computation and Discussion

The experimental FLDs of the present analysis, involve the experimental forming limits obtained for linear strain paths (LSP) namely, uniaxial tension (UT), plane strain (PS) and biaxial stretching (BS) with circular and elliptical die rings, and for complex strain paths namely, uniaxial tension followed by biaxial stretching (UT-BS), biaxial stretching followed by uniaxial tension (BS-UT), uniaxial tension followed by stretching with different elliptical die rings (UT-X).

It is known that the geometric defect of the MK analysis is conventional and not a real physical attribute of the specimen. However, choosing a unique value of the imperfection factor for all models could have biased the comparison, by favouring one model or another. Therefore, we have chosen here an alternative approach, which seems better justified in this case: the imperfection factor has been slightly varied for each model, until the best agreement with the experimental data has been found. Subsequently, these best individual results have been used to compare the models.

Figures 3, 4, 5, 6 and 7 show the experimental forming limits for the DC06 steel sheet under proportional and non-proportional loading and the computed ones, when the strain hardening is defined by the five hardening models considered in this paper. In order to achieve the best agreement with the experimental data, the initial value of the M-K geometrical defect was individually selected for each case, namely 0.996 for MicMod, 0.9915 for Swift, 0.993 for Swift +KH, 0.998 for Voce and 0.9975 for Voce + KH.

Inspection of these figures reveals a particularly good agreement between theoretical and experimental forming limits for the selected material, under linear and complex strain paths, when MicMod is used. It may be reasonably assumed that this remarkable accuracy in the FLD prediction is due to the relevance of the applied constitutive model for the DC06 steel.

The right-hand side of the FLD under linear strain paths is correctly predicted by all hardening models. Concerning the left –hand side of the FLD an overestimation on the predicted forming limits is noticed when the Swift law with and without kinematic hardening is used, whereas a considerable underestimation on the predicted FLDs is noticed when the Voce law with and without kinematic hardening is used. Most probably, these results are a consequence of the overestimation, respectively the underestimation of the hardening behaviour, as previously noticed by Barlat *et al.* (2006)

As usual, the lowest forming limit under proportional loadings is obtained for the plane strain deformation state. The plastic flow instability occurs when a through-thickness neck forms in the sheet, as already pointed out by Stoughton and Yoon (2006). According to the study on plastic flow localisation developed by Barlat and Lian (1989) based on the MK analysis, under plane strain deformation state, the thickness imperfection growth is smaller than in uniaxial tension and biaxial stretching, because it is counterbalanced only by the strain hardening, while during the other strain paths is counterbalanced both by the strain hardening and by the so-called “yield surface shape hardening”. A good prediction of the FLD under plane strain state is obtained by all considered models.

Concerning the strain path changes, it is remarkable that all hardening models predict the increase of formability after uniaxial tension followed by equibiaxial stretching (UT-BS), as well as the loss of formability after equibiaxial stretching followed by uniaxial tension (BS-UT), although these two deformation histories have the same value of the parameter introduced by Schmitt *et al.* (1985) to characterize the strain-path changes (namely 0.269). Actually, the earlier appearance of plastic instability under the sequence BS-UT may be attributed to the fact that the second path is the uniaxial tension, which is more sensitive to strain localization. For UT-BS, the balanced biaxial

stress state leads to a very stable strain path (meaning that it is possible to deform the material up to high strains without localized necking). According to Fernandes and Schmitt (1983) the through-thickness strain after the same amount of equivalent strain under equibiaxial stretching is lower than after uniaxial tension. Hence, a through–thickness neck followed by plastic localization appears earlier under equibiaxial stretching prestrains than under uniaxial tension prestrains. This also influences the moment of the occurrence of plastic localization under UT-BS and BS-UT.

The accuracy of the predicted FLDs is good for all models under UT-BS. On the contrary, in the case of BS-UT strain-path change, only the MicMod model reproduces correctly the experimental data, while a considerable overestimation of the FLDs is noticed when using the Swift or Voce hardening laws, with and without kinematic hardening.

All the phenomenological models predict the lowest curve on the FLD the curve obtained for biaxial stretching followed by plane strain sequence (acronym BS-PS), with a Schmitt et al. factor equals to 0.889. Besides its great ability on predicting accurate FLDs, the microstructural hardening model uniquely reproduces the experimental Nakazima tendency for the considered steel, by predicting for the BS-UT sequence the lowest curve on the forming limit diagram. Hiwatashi *et al.* (1998) and Hoferlin *et al.* (1998) ascribed such drop in formability to the interaction between the currently active slips and the previously formed dislocation structures, as suggested by Rauch and Schmitt (1989) in their experimental work. Actually, this phenomenon is very well described by the microstructural hardening model, being captured through its internal variables.

Figure 8 summarizes the strain paths during UT prestraining and subsequent FLD tests consisting in the variation of the strain ratio simulating a strain-path range between UT and BS.

Figures 9, 10, 11, 12 and 13 show experimental and theoretical FLDs for the DC06 steel sheet determined under non-proportional loading by using a sequence of two linear strain paths (UT-X), keeping constant the preliminary strain ratio and the amount of prestrain and varying the subsequent strain ratio, while defining the strain hardening by

the models: (*i*) MicMod; (*ii*) Swift; (*iii*) Swift + KH; (*iv*) Voce; (*v*) Voce + KH. In all cases, a reasonable proximity of the predicted curves to the experimental points obtained by a uniaxial prestrain of 7%, respectively 14%, followed by stretching with an elliptical matrix, is observed. The tensile prestrain along RD shifts the whole FLD to the left, raising the strain limits in biaxial tension region and consequently increasing the slope of right–hand side of the FLD. The same effect produced by a tensile prestrain on the FLDs was previously noticed by Graf *et al.* (1993) and Butuc *et al.* (2003).

4.3 Influence of the back stress on forming limits prediction

As previously mentioned, in this work the back stress was calculated using the classical Armstrong-Frederick law, as well as a modified version of this law included in the microstructural hardening model, which assumes that the saturation value of the kinematic hardening depends on the strength of the dislocation structures through the internal state variable $\boldsymbol{S}$ (cf. Eq. (7)). In what follows, a sensitivity analysis of the influence of back stress on the predicted forming limits will be presented.

Figure 14 shows the evolution of the back stress normalized by the saturation value X_{sat} under uniaxial tension at 0º from RD, in the case of the models (*i*) MicMod, (*ii*) Swift+KH, and (*iii*) Voce +KH. It is noticed that $\boldsymbol{X}$ evolves progressively with the straining and saturates at X_{sat} according to its saturation rate C_X. Hence, in the case of microstructural hardening model and of the Swift law, due to the relatively large numerical values of C_X, namely 446 and 446.9, respectively, the normalized back stress saturates faster than in the case of Voce law, which is characterized by a much lower value of C_X, namely $C_X = 163$.

Figure 15 shows the influence of back stress on forming limits by comparing the predicted FLDs when the strain hardening is defined by the Swift law with and without kinematic hardening. A single geometrical defect value of 0.9915 is used in these simulations. Under linear strain-path loading, it is noticed that in the case of Swift law with kinematic hardening the strain limits predicted in the uniaxial tension and the biaxial stretching zones are lower than in the case of the Swift law without kinematic hardening. Consequently, the presence of the back stress contributes to a decrease by 2% and 2.5%, respectively, in the forming limits under UT and BS. The same effect is

noticed under UT-BS, where a decrease by 3% of the forming limits is observed when the back stress is taken into account. On the contrary, under BS prestrain, followed either by UT or by PS deformation, the presence of the back stress contributes to an increase around 1.5% in the predicted forming limits. In the case of a BS prestrain followed by stretching with different elliptical die rings (expressed here by different values of the stress ratio α) a slight variation of the increase of predicted forming limits has been found. Explicitly, for $\alpha = 0.7$ the increase of forming limits predicted by Swift law with kinematic hardening varies between 0.2% and 2.2%, for $\alpha = 0.8$ it varies between 0.4 % and 1.3%, while for $\alpha = 0.9$ it varies merely between 0.1% and 0.9%. It can be concluded that the back stress influences the predicted forming limits, whereas the respective values of the increase and decrease of the forming limits are relatively low.

Figure 16 shows the influence of back stress on the FLDs, by comparing the predicted FLDs when the strain hardening is defined by the Voce law with or without kinematic hardening. In this case the used geometrical defect value is 0.998. Under linear and complex strain paths, it may be noticed an increase in the predicted forming limits when the back stress is taken into account. Explicitly, such increase takes the following values depending on the assumed strain path: 10% for UT, 2.6% for BS, 4.5% for BS-UT, between 5% and 9% for UT-BS and 2.3% for BS-PS. For a biaxial stretching prestrain, followed by stretching with different elliptical die rings (acronym BS-α), the forming limits increase between 4.9% and 1.3% for BS-$\alpha = 0.7$, between 4.9% and 1.5% for BS-$\alpha = 0.8$ and between 4.3% and 3.3% for BS-$\alpha = 0.9$. Clearly, in all these cases, the influence of the back stress on the predicted forming limits decreases with the increase of the biaxial prestrain values.

By comparing the results of Figures 15 and 16, it may be seen that the back stress has a more pronounced effect on the FLDs in the case of the Voce law than in the case of the Swift law. This result may be reasonably attributed to the difference in the variation of the slopes and of the curvatures of the stress-strain curves approximated with and without back stress, being smaller for the Swift law than for the Voce law.

5. CONCLUSIONS

Several hardening models, namely the microstructural hardening model of Teodosiu and Hu, the Swift law with and without kinematic hardening, and the Voce law with and without kinematic hardening, coupled with the Yld2000-2d yield function have been used to predict the forming limits for DC06 steel sheet under linear and two types of strain path changes.

The right-hand side of the FLD under linear strain paths is correctly predicted by all hardening models. The left-hand side of the FLD is overestimated when Swift with/without kinematic hardening is used and underestimated when Voce with/without kinematic hardening is used. In the case of the microstructural hardening model a particularly good agreement between the predicted and experimental forming limits was observed.

All hardening models predicted the increase of formability after uniaxial tension followed by equibiaxial stretching (UT-BS), as well as the loss of formability after equibiaxial stretching followed by uniaxial tension (BS-UT). The appearance of plastic instability under the BS-UT sequence is most probably due to the fact that the second strain path is a uniaxial tension and hence subject to geometrical instabilities. On the contrary, for the sequence UT-BS, the balanced biaxial stress state leads in the second path to a very stable deformation not subjected to geometrical instabilities.

The accuracy in predicting the loss of formability under biaxial prestrain followed by uniaxial tension is strictly connected with the accuracy of the hardening model to reproduce the hardening behaviour under this strain-path change. It is noteworthy that, among the considered hardening models, solely the Teodosiu-Hu model is able to reproduce the Nakazima experimental tendency. Such additional drop in formability under biaxial prestrain followed by uniaxial tension is possibly a consequence of the interaction between the currently active slips and the previously formed dislocation structures, a phenomenon which is well captured by the microstructural hardening model through its internal variables.

A sensitive study of the effect of the back stress on the occurrence of the plastic flow localization was performed. It was found that the effect of the back stress on the

prediction of forming limits under linear and complex loadings depends on the assumed type of hardening model.

Acknowledgement: The authors thank the Laboratory of the Mechanical and Thermodynamic Properties of the Materials (LPMTM) of the University Paris 13, France, for providing the material parameters of the hardening models used in the paper.

References

3DS Report, 2001. Selection and identification of elastoplastic models for the materials used in the benchmarks. 18-Months Progress Report, International IMS Research Contract "Digital Die Design Systems (3DS)", Laboratory of the Mechanical and Thermodynamic Properties of the Materials, University Paris 13, Villetaneuse, France.

Armstrong, P.J., Frederick, C.O., 1966. A mathematical representation of the multiaxial Bauschinger effect. GEGB Report RD/B/N731, Berkeley Nuclear Laboratories.

Barlat F. and Lian, J., 1989. Plastic behavior and stretchability of sheet metals. Part I: A yield function for orthotropic sheets under plane stress conditions. Int. J. Plasticity 5, 51-66.

Barlat F., Maeda Y., Chung K., Yanagawa M., Brem J.C., Hayashida Y., Lege D.J., Matsui K., Murtha S.J., Hattori S., Becker R.C., Makosey S., 1997. Yield function development for aluminium alloy sheets. J. Mech. Phys. Solids. 45, 1727-1763.

Barlat, F., Brem, J. C., Yoon, J. W., Chung, K., Dick, R. E., Lege, D. J., Pourboghrat, F., Choi, S. -H. Chu E., 2003. Plane stress yield function for aluminum alloy sheets. Part 1: theory. Int. J. Plasticity 19, 1297-1319.

Barlat F., Yoon, J:W., Cazacu, O., 2007. On linear transformations of stress tensors for the description of plastic anisotropy. Int. J. Plasticity 23, 876-896.

Barlat, F., Brem, J.C., Yoon, J.W., 2006. Strain hardening approximation for aluminum alloy sheets. In: Anisotropy, Texture, Dislocations and Multiscale Modeling in Finite Plasticity & Viscoplasticity, and Metal Forming, Proc. Plasticity'06, The Twelfth International Symposium on Plasticity and its Current Applications, A.S. Khan, R. Kazmi (Eds.), Halifax, Nova Scotia (Canada), July 17-22, pp. 4-6.

Bouvier S., Haddadi H., Levée P., Teodosiu C., 2006a. J. Mater Process Tech 172, 96-103.

Bouvier S., Gardey B., Haddadi H., Teodosiu C., 2006b. J. Mater Process Tech 174, 115-126.

Butuc, M.C., Gracio, J.J., Barata da Rocha, A., 2003. A theoretical study on forming limit diagrams predictions. J. Mater. Process. Tech. 142, 714-724.

Butuc, M.C, 2004. Forming limit diagrams. Definition of plastic instability criteria. PhD. Thesis, Porto University.

Fernandes J.V., Schmitt J.-H., 1983. Dislocation microstructures in steel during deep drawing. Philosophical Magazine A48, 841-870

Goodwin, G.M., 1968. Application of strain analysis to sheet metal forming problems in the press shop. Society of Automotive Engineers, Technical Paper No. 680093.

Graf A., Hosford W. F., 1993. Effect of changing strain paths on forming limit diagrams of Al 2008-T4. Metallurgical and Materials Transactions A24, 2503.

Haddadi, H., Bouvier, S.. Banu, M., Maier, C., Teodosiu, C., 2006. Towards an accurate description of the anisotropic behaviour of sheet metals under large plastic deformations: Modelling, numerical analysis and identification. Int. J. Plasticity 22, 2226-2271.

Hashiguchi K., Protasov A., 2004. Localized necking analysis by the subloading surface model with tangential-strain rate and anisotropy. . Int. J. Plasticity 20, 1909-1930.

Hiwatashi, S., Bael, A.V., Houtte, P.V., Teodosiu, C., 1998. Prediction of forming limit strains under strain path changes: application of an anisotropic model based on texture and dislocation structure. Int. J. Plasticity 14, 647-669.

Hoferlin E., Van Bael A., Hiwatashi S., Van Houtte P., 1998. Influence of texture and microstructure on the prediction of forming limit diagrams. In Proc. of the 19th Riso Inter. Symposium on Materials Science: Modelling of Structure and Mechanics of Materials from Microscale to Product, J.V. Cartensen et al. (Eds.), Danemark, pp. 291-297.

Keeler S.P., 1965. Determination of forming limits in automotive stampings. Society of Automotive Engineers, Technical Paper No. 650535.

Lu Z.H., Lee D., 1987. Prediction of history-dependent forming limits by applying different hardening models. Int. J. Mech. Sci. 29, 123-137.

Marciniak, Z., Kuczynski, K., 1967. Limit strains in the processes of stretch-forming sheet metal. Int. J. Mech. Sci. 9, 609-620.

Nakazima K., Kikuma T., Hasuka, 1968. Study on the formability of steel sheets. Yawata Technical Report, No. 264, pp. 141-154.

Rauch E. F. and Schmitt J.-H., 1989. Dislocation substructure in mild steel deformed in simple shear. Mater. Sci. Eng. A113, 441-448.

Signorelli, J.W., Bertinetti, M.A., Turner, P.A., 2009. Predictions of forming limit diagrams using a rate-dependent polycrystal self-consistent plasticity model. Int. J. Plasticity 25, 1-25.

Stoughton, T.B., Zhu, X., 2004. Review of theoretical models of the strain-based FLD and their relevance to the stress-based FLD. Int. J. Plasticity 20, 1463-1486.

Stoughton, T.B., Yoon, J.W., 2006. Review of Drucker's postulate and the issue of plastic instability in metal forming. Int. J. Plasticity 22, 391-433.

Teodosiu C., Hu Z., 1995. Evolution of the intragranular microstructure at moderate and large strains: Modelling and computational significance. In: S.-F. Shen, P.R. Dawson (Eds), Proc. NUMIFORM' 95, pp. 173-182.

Tvergaard V.,1978. Effect of kinematic hardening on localized necking in biaxially stretched sheets. Int. J. Mech. Sci. 20, 651-658

Van Houtte, P., Van Bael, A., Winters, J., 1995. The incorporation of texture-based yield loci into elasto-plastic finite element programs. Textures and Microstructures 24, 255-272.

Yao H. and Cao J. 2002. Prediction of forming limit curves using an anisotropic yield function with prestrain induced back stress. Int. J. Plasticity. 18(8), 1013-1038.

Appendix.

MK theoretical calculation of the occurrence of localized necking

The adopted algorithm is incremental. Its main objective is to find the stress and strain tensors in the current state for a given equivalent strain increment. This algorithm is presented for one loading condition and a single value of ψ_0, the initial orientation of geometrical defect. By imposing to the homogeneous part small increments of the equivalent strain $\bar{\varepsilon}^a$ and the stress ratio α^a characterizing the assumed strain path, the corresponding strain and stress state are computed as follows:

- Computation of the initial stress tensor σ_{ij}^{0a}, by imposing the stress direction and applying the yield function and Euler theorem of homogeneous functions
- Computation of the initial deviatoric stress $\boldsymbol{\sigma}'^{0\,a}_{ij}$
- Conversion of deviatoric stress $\boldsymbol{\sigma}'^{0\,a}_{ij}$ from 3 x 3 component notation in five-dimensional vector notation $\boldsymbol{\sigma}'^{0\,a}_{I}$ (see Butuc, 2004)
- Computation of the initial strain rate tensor through the plastic flow equations:

$$D^a{}_{ij} = \dot{\bar{\varepsilon}}^a * \partial\sigma^a \big/ \partial\sigma'_{ij}{}^a \tag{A.1}$$

The strain rate tensor $\boldsymbol{D}^{\boldsymbol{a}}$ is assumed to be constant during an increment and it is represented as:

$$\boldsymbol{D}^a = \begin{bmatrix} D_{11}^a & 0 & 0 \\ 0 & D_{22}^a & 0 \\ 0 & 0 & -D_{11}^a - D_{22}^a \end{bmatrix} \tag{A.2}$$

with $D_{11}^a > 0$ and $D_{11}^a \geq D_{22}^a$ (A.3)

- Calculation of the actual plastic strain rate direction $\boldsymbol{A}^a$:

$$\boldsymbol{A}^a = \boldsymbol{D}^a \big/ \sqrt{\boldsymbol{D}^a : \boldsymbol{D}^a} \tag{A.4}$$

- Conversion of $\boldsymbol{A}^{a}$ from 3 x 3 component notation in a five-dimensional vector notation

- Computation of the internal variables $\boldsymbol{S}^{a}, \boldsymbol{P}^{a}, \boldsymbol{X}^{a}, R^{a}$ and of the yield stress $\bar{\sigma}_{\boldsymbol{Y}}^{a}$ through the microstructural hardening model in the case of MicMod.

- Computation of the yield stress $\bar{\sigma}_{\boldsymbol{Y}}^{a}$ through the assumed hardening model in the case of the models Swift + KH, Voce + KH, Swift, Voce.

- Computation of the back stress tensor $\boldsymbol{X}^{a}$ according to Eq. 19 for the cases of Swift + KH, Voce +KH.

- For the purpose of clarity, $\boldsymbol{\Sigma}^{\mathbf{a}}$ will denote in the following the effective deviatoric stress tensor expressed by:

$$\boldsymbol{\Sigma}^{\mathbf{a}} = \boldsymbol{\sigma}'^{a} - \mathbf{X}^{\mathbf{a}} \tag{A.5}$$

- Computation of the equivalent effective stress $\bar{\sigma}_{\boldsymbol{e}}^{a}$ through the yield function.

$$\bar{\sigma}_{e}^{a} = \left(\phi\left(\boldsymbol{\Sigma}^{a}\right)/2\right)^{1/a} \tag{A.6}$$

- Computation of the actual stress tensor $\sigma_{\boldsymbol{ij}}^{a}$ through the Newton-Raphson method on the base of yield condition:

$$F \equiv \bar{\sigma}_{e}^{a} - \bar{\sigma}_{Y}^{a} = 0 \tag{A.7}$$

The Newton-Raphson solution gives:

$$\Sigma_{11}^{a} = \Sigma_{11}^{a} - F(\Sigma_{11}^{a}) / DF(\Sigma_{11}^{a}) \tag{A.8}$$

where $F(\Sigma_{11}^{a})$ represents the yield criteria expressed as a function of Σ_{11}^{a}, and *DF* the first derivative of *F*. Knowing the effective deviator stress tensor and the backstress, the stress tensor $\boldsymbol{\sigma}^{a}$ may be found.

- Update of the final strain rate tensor through the plastic flow equations, using final deviatoric stress tensor σ'^{a}_{ij} and the yield stress $\bar{\sigma}_{Y}$.

$$D_{ij}^{a} = \dot{\bar{\varepsilon}}^{a} * \partial \bar{\sigma}^{a} / \partial \left({\sigma_{ij}}'^{a} - X_{ij}^{a} \right) \tag{A.9}$$

- Computation of the strain tensor by the time integration of strain rate tensor

$$d\varepsilon_{ij}^{a} = \int_{t}^{t+\Delta t} D_{ij}^{a} dt \tag{A.10}$$

- By a change of axes, the stress and strain states in the groove reference frame namely $\boldsymbol{\sigma}_{ntz}^{a}$ and $d\boldsymbol{\varepsilon}_{ntz}^{a}$ are computed.

Concerning the identification of stress and strain state in the imperfection region, there are two unknowns, namely the equivalent incremental strain $d\bar{\varepsilon}^{b}$ and the stress value in the longitudinal direction of the groove σ_{tt}^{b}. In order to identify them, the Newton-Raphson method is again applied.

The current imperfection value f is characterized by the ratio of the sheet thickness in regions A and B and is expressed as a function of the initial defect f_0 as

$$f = f_0 \exp\left(\varepsilon_3^{b} - \varepsilon_3^{a} \right). \tag{A.11}$$

The condition of force equilibrium between zones A and B allows calculating the flow stress value in the normal direction of the groove and the flow shear stress in the groove as

$$\sigma_{nn}^{b} = \sigma_{nn}^{a} / f, \tag{A.12}$$

$$\sigma_{nt}^{b} = \sigma_{nt}^{a} / f . \tag{A.13}$$

Then, the components of the stress tensor $\boldsymbol{\sigma}^{b}$ in the orthotropic axes of anisotropy may be obtained by a straightforward calculation.

The yield stress $\bar{\sigma}_{Y}^{b}$ and the back stress tensor $\boldsymbol{X}^{b}$ are computed for each of the selected hardening models by using the same procedure as that already presented for the homogeneous part. After the computation of the effective deviator stress tensor $\boldsymbol{\Sigma}^{b}$, the equivalent effective stress $\bar{\sigma}_{e}^{b}$ is evaluated through the yield function.

$$\bar{\sigma}_e^b = \left(\phi\left(\boldsymbol{\Sigma}^b\right)/2\right)^{\frac{1}{a}} \tag{A.14}$$

Applying the flow rule, the strain rate tensor $\boldsymbol{D}^b$ and consequently the strain matrix increment in the imperfection region $d\boldsymbol{\varepsilon}^b$ in the orthotropic referential frame of anisotropy is determined. This allows expressing the yield criterion and the deformation compatibility requirement in the longitudinal direction of the necking band, by two nonlinear equations in $d\bar{\varepsilon}^b$ and σ_{tt}^b:

$$G_1\left(d\bar{\varepsilon}^b, \sigma_{tt}^b\right) = \bar{\sigma}_Y^b - \bar{\sigma}_e^b = 0 \tag{A.15}$$

$$G_2\left(d\bar{\varepsilon}^b, \sigma_{tt}^b\right) = d\varepsilon_{tt}^a - d\varepsilon_{tt}^b = 0 \tag{A.16}$$

where G_1 and G_2 are two polynomial functions of $d\bar{\varepsilon}^b$ and σ_{tt}^b.

By using Eqs (A.15) and (A.16), the iterative formula for Newton-Raphson's method may be written as

$$\begin{bmatrix} d\bar{\varepsilon}^b{}_{i+1} \\ \sigma_{tt\,i+1}^b \end{bmatrix} = \begin{bmatrix} d\bar{\varepsilon}^b{}_i \\ \sigma_{tt\,i}^b \end{bmatrix} - J^{-1} \begin{bmatrix} G_1\left(d\bar{\varepsilon}^b{}_i, \sigma_{tt\,i}^b\right) \\ G_2\left(d\bar{\varepsilon}^b{}_i, \sigma_{tt\,i}^b\right) \end{bmatrix} \tag{A.17}$$

where J^{-1} is the inverse of the Jacobian matrix J, which is defined, as usual, by the partial derivatives of functions G_1 and G_2 with respect to $d\bar{\varepsilon}^b$ and σ_{tt}^b .

If the failure condition is not satisfied, the computation continues after the update of the internal variables and after determining the current value of ψ defining the actual position of the groove by

$$\mathrm{tg}\psi = \left(\mathrm{tg}\psi_0\right)\exp\left(\varepsilon_{11}^a - \varepsilon_{22}^a\right). \tag{A.18}$$

Research Highlights

> An advanced model is used to predict the forming limits for DC06 steel sheet. **>** Several isotropic and non-linear kinematic hardening models are selected. **>** Microstructural hardening model reproduces correctly the experimental results. **>** Geometrical instabilities influence the plastic instability under complex loadings. **>** The type of hardening model influences the back stress effect on the FLDs prediction.

Table 1. DC06 steel uniaxial tensile properties at 0º, 45º and 90º from rolling direction

Orientation	Yield stress [MPa]	Ultimate tensile strength σ_{uts} [MPa]	Uniform elongation	Anisotropy factor *r*
0º	136	374	29%	2.6
45º	134	369	27%	2.1
90º	136	365	28%	3.2

Table 2. The values of σ_b and r_b

Material parameter	DC06 steel
σ_b [MPa]	142.204
r_b	0.81

Table 3. The coefficients of the Yld00-2d yield function

Material	*a*	α_1	α_2	α_3	α_4	α_5	α_6	α_7	α_8
DC06 steel	6	1.055	1.09	1.00	0.9	0.937	1.056	1.069	0.926

Table 4. Material parameters of the microstructural model

Parameters	DC06 steel
Y_0	121.1 MPa
C_R	31.9
R_{sat}	90.0 MPa
C_X	446
X_0	15.9 MPa
C_{SD}	4
C_{SL}	1.86
S_{sat}	231.1 MPa
n_L	0
n_p	27.9
q	1.5
m	0.445
C_P	5.5

Table 5. Material parameters of the Swift hardening law with and without kinematic hardening

Isotropic hardening Swift law		Isotropic hardening Swift law + kinematic hardening	
Y_0	124.7 MPa	Y_0	121.1 MPa
ε_0	0.00385	ε_0	0.00224
n	0.257	n	0.221
C	522.0	C	446.9
		C_X	1.87
		X_{sat}	58.1 MPa

Table 6. Material parameters of the Voce hardening law with and without kinematic hardening

Isotropic hardening Voce law		Isotropic hardening Voce law+ kinematic hardening	
Y_0	124.7 MPa	Y_0	121.1 MPa
C_R	12.1	C_R	7.3
R_{sat}	250.5	R_{sat}	236.5
		C_X	153.3
		X_{sat}	49 MPa

Table 7. The experimental and predicted normalized yield stress and anisotropy factors

Orientation	Yield stress σ_Y/σ_0 Experimental	Yield stress σ_Y/σ_0 Predicted	Anisotropy factor r Experimental	Anisotropy factor r Predicted
0º	1	1	2.6	2.6
45º	0.985	0.985	2.1	2.1
90º	1.0	1.0	3.2	3.2
BB	1.045	1.045	0.8104	0.8104

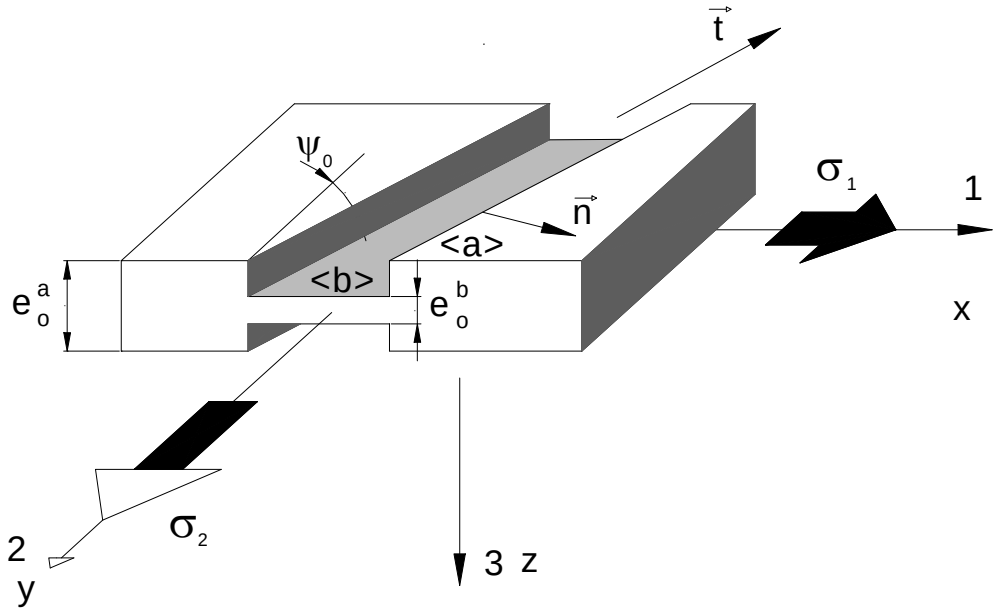

Fig. 1. Initial geometrical imperfection of the M-K analysis

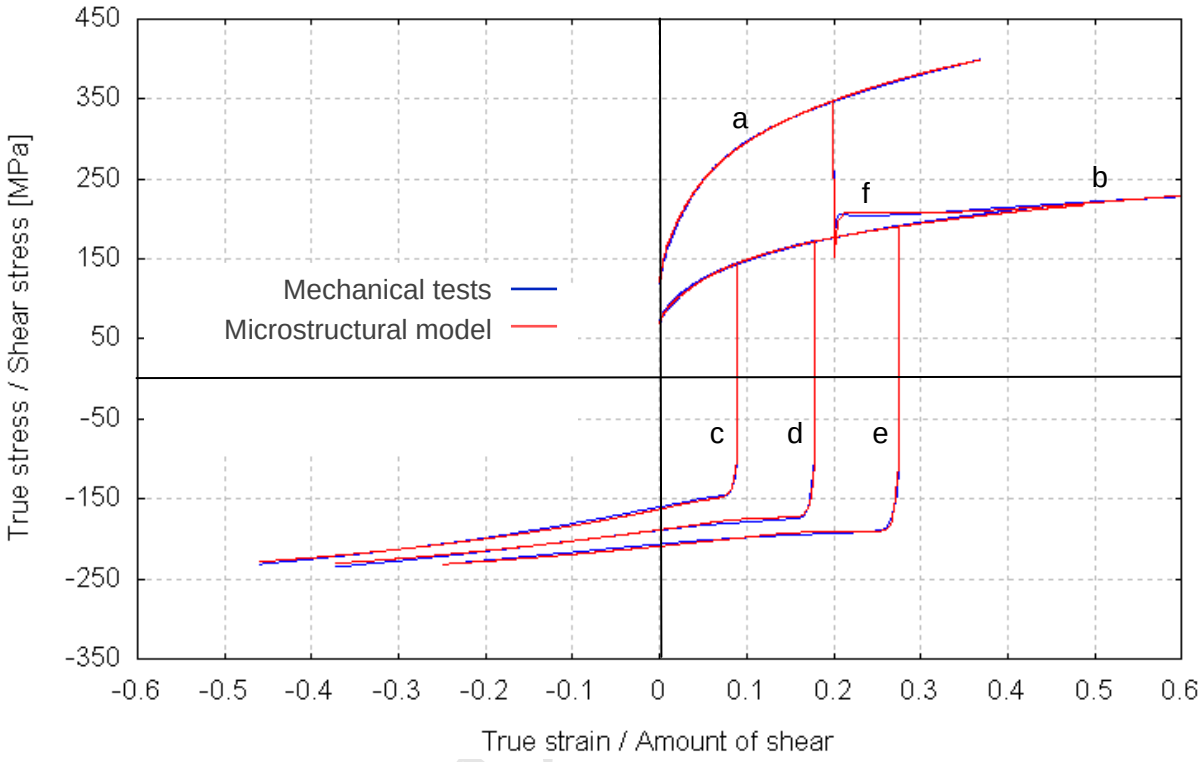

Fig. 2a. Comparison of the results of mechanical tests with the prediction of the microstructural model for the mild IF-steel DC06 (after 3DS Report, 2001). (a) Uniaxial tensile test. (b) Monotonic simple shear along the rolling direction. (c), (d), (e) Bauschinger simple shear along the rolling direction after 10%, 20% and 30% amount of shear in the forward direction, respectively. (f) Orthogonal test: simple shear in the rolling direction after 20% true tensile strain in the same direction.

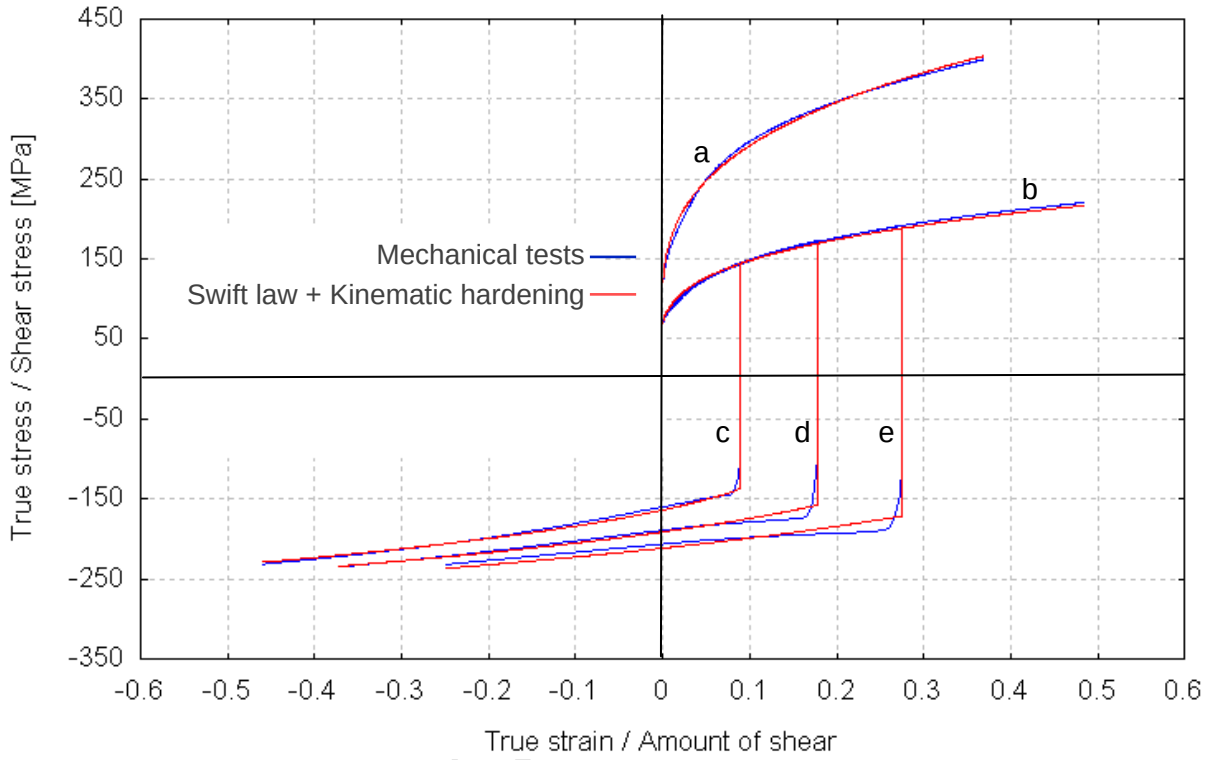

Fig. 2b. Comparison of the results of mechanical tests with the prediction of the model combining the Swift isotropic hardening with non-linear kinematic hardening for the mild IF-steel DC06 (after 3DS Report, 2001). (a) Uniaxial tensile test. (b) Monotonic simple shear along the rolling direction. (c), (d), (e) Bauschinger simple shear along the rolling direction after 10%, 20% and 30% amount of shear in the forward direction, respectively.

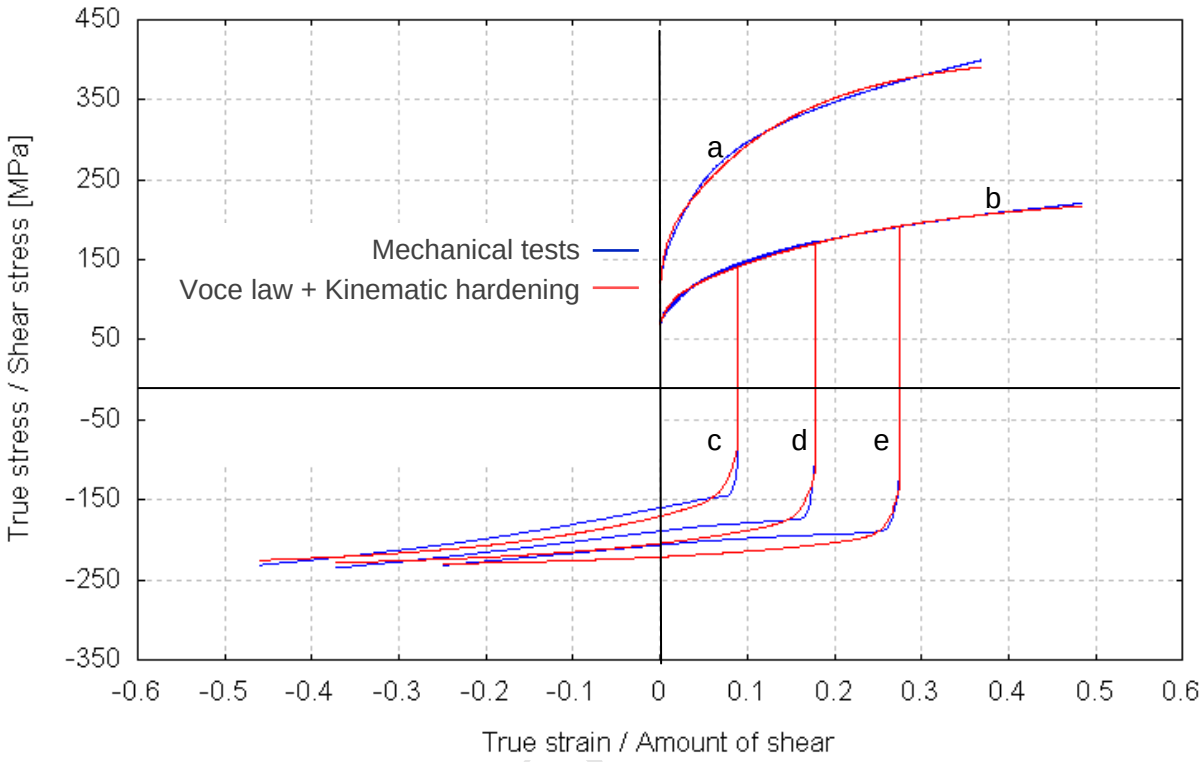

Fig. 2c. Comparison of the results of mechanical tests with the prediction of the model combining the Voce isotropic hardening with non-linear kinematic hardening for the mild IF-steel DC06 (after 3DS Report, 2001). (a) Uniaxial tensile test. (b) Monotonic simple shear along the rolling direction. (c), (d), (e) Bauschinger simple shear along the rolling direction after 10%, 20% and 30% amount of shear in the forward direction, respectively.

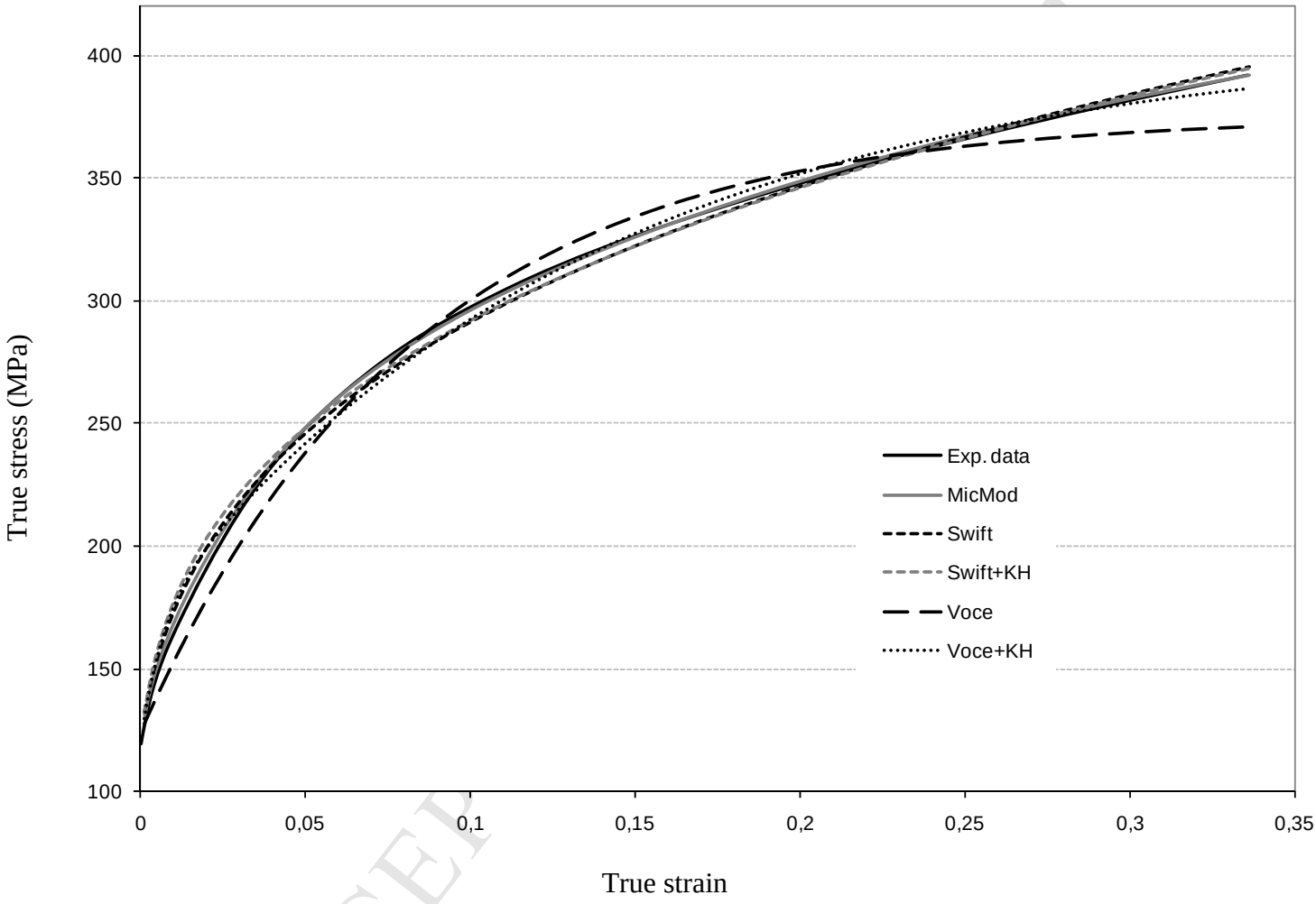

Fig. 2d. Experimental and predicted stress-strain curves for the DC06 steel sheet specimen under uniaxial tension at 0º from RD.

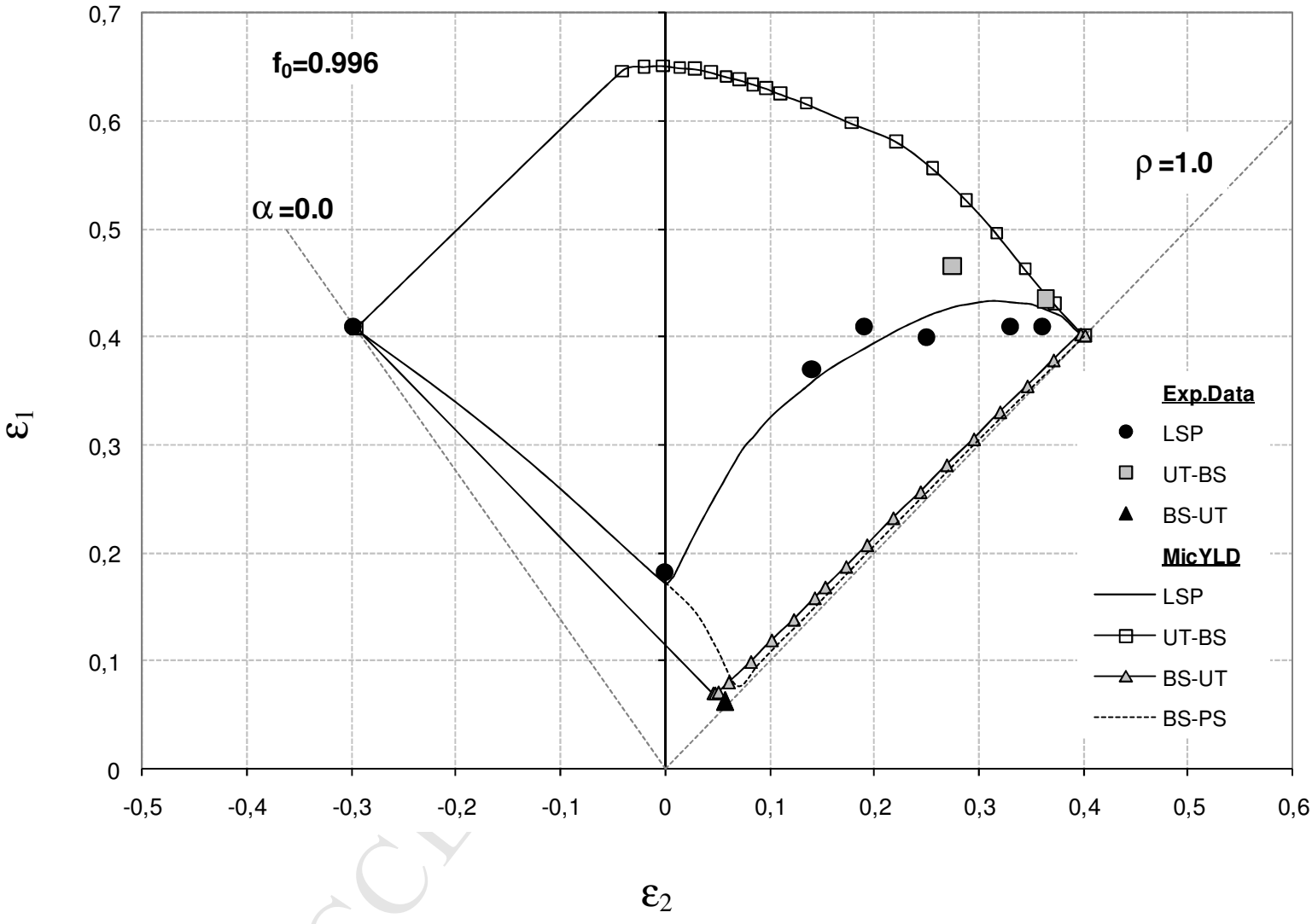

Fig. 3. Experimental and theoretical FLDs under linear and complex strain paths for DC06 steel sheet, using the microstructural hardening model and YLD2000-2d yield function.

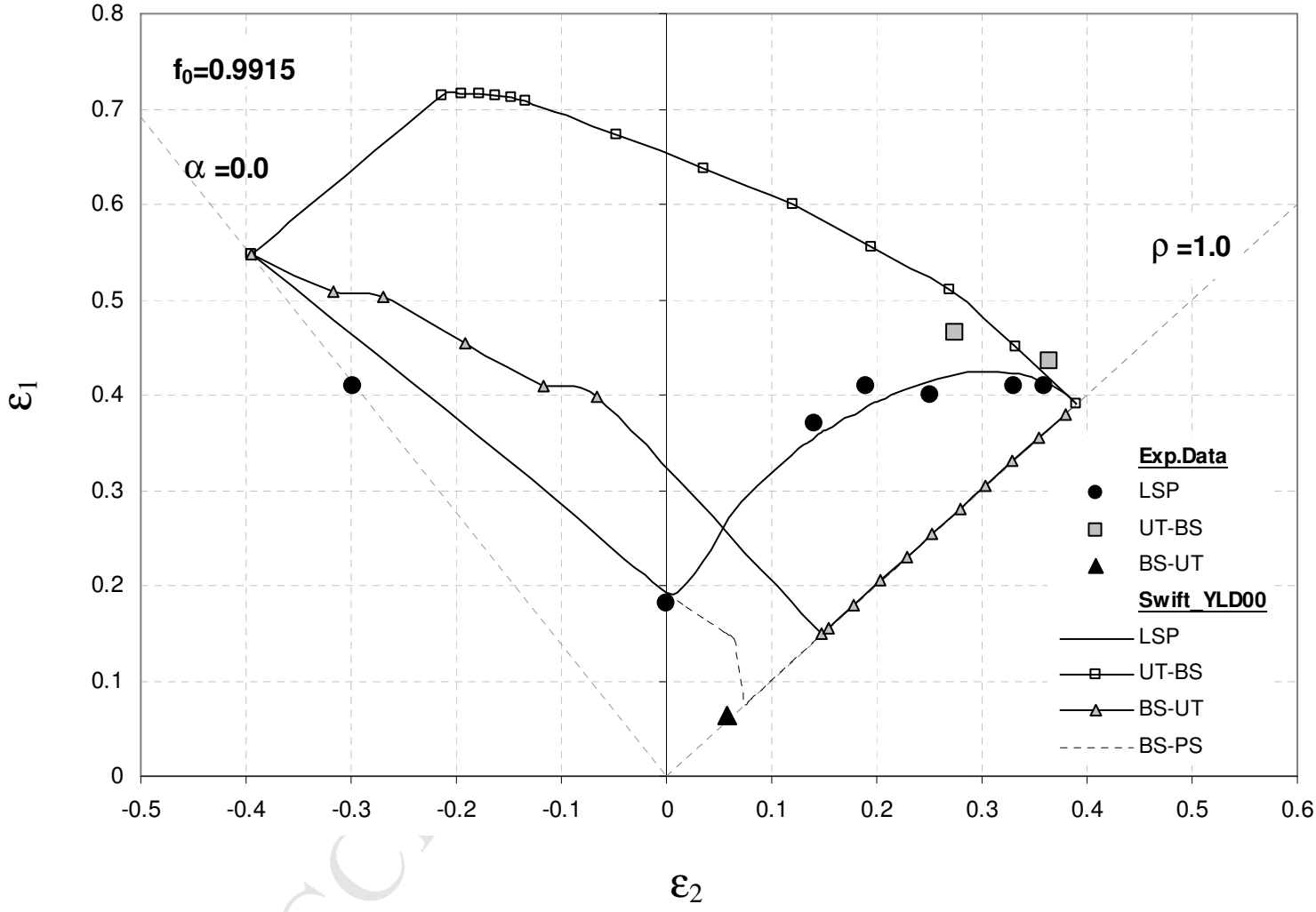

Fig. 4. Experimental and theoretical FLDs under linear and complex strain paths for the DC06 steel sheet, using Swift law and the YLD2000-2d yield function.

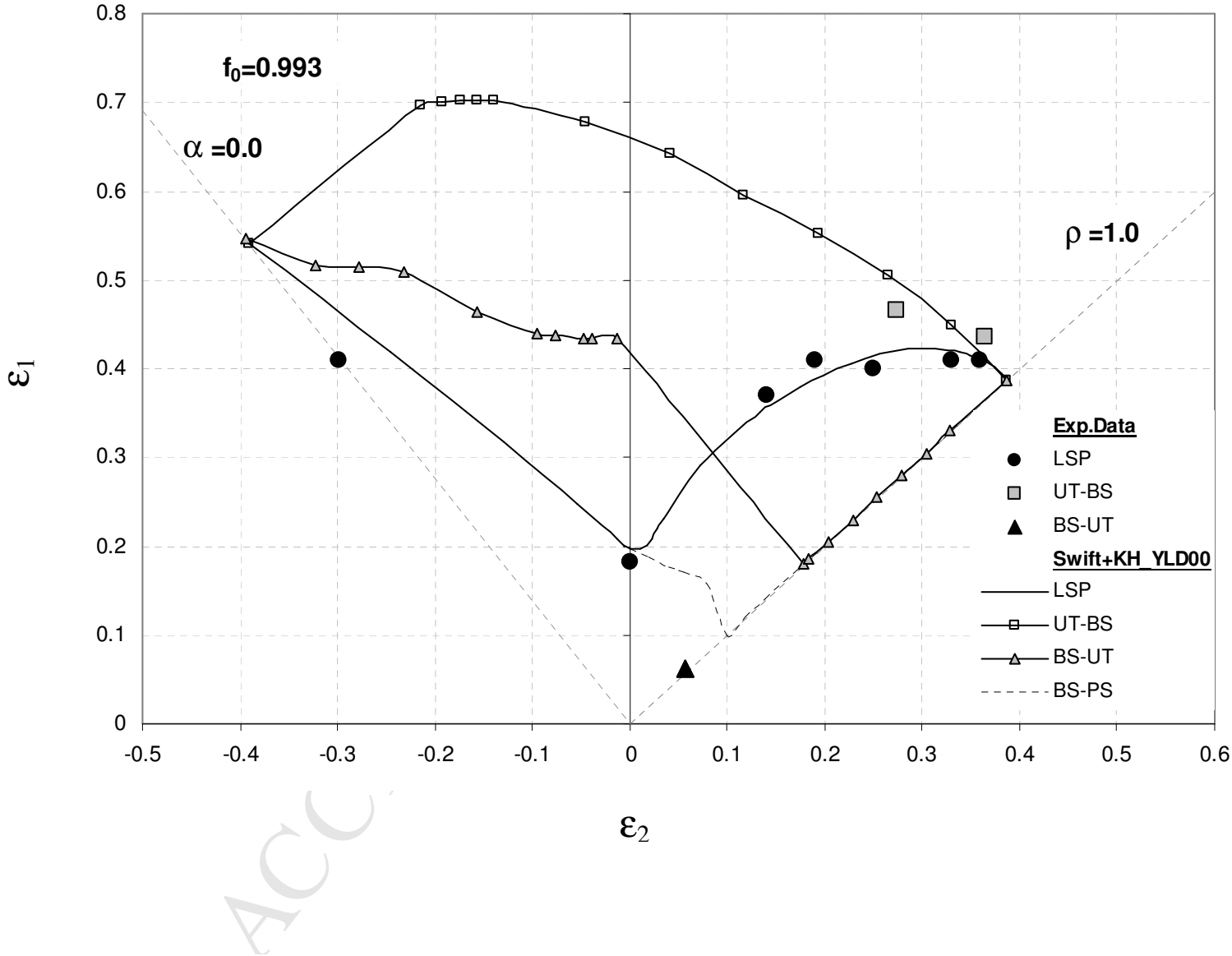

Fig. 5. Experimental and theoretical FLDs under linear and complex strain paths for DC06 steel sheet, using Swift law + kinematic hardening and YLD2000-2d yield function.

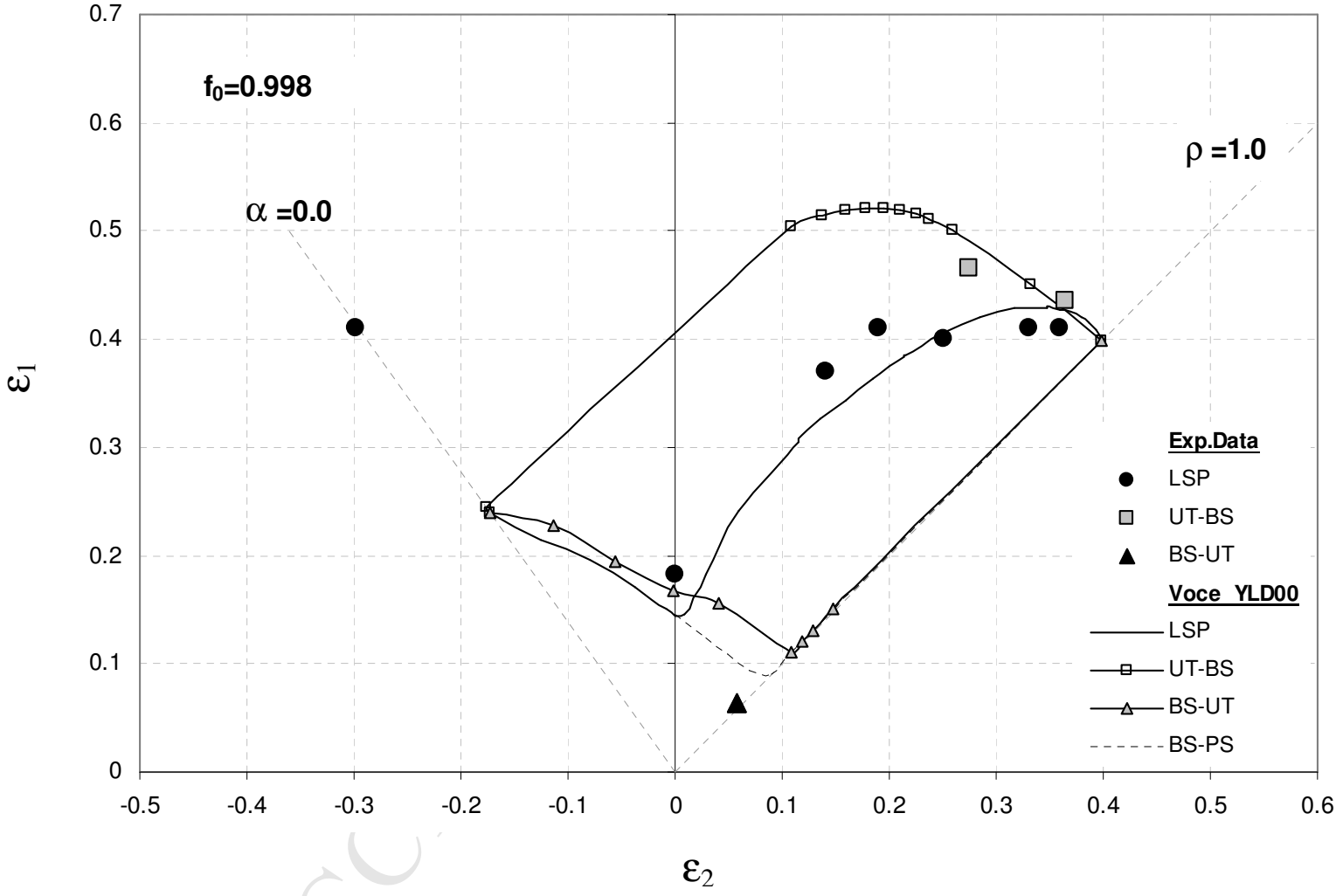

Fig. 6. Experimental and theoretical FLDs under linear and complex strain paths for DC06 steel sheet, using Voce law and YLD2000-2d yield function.

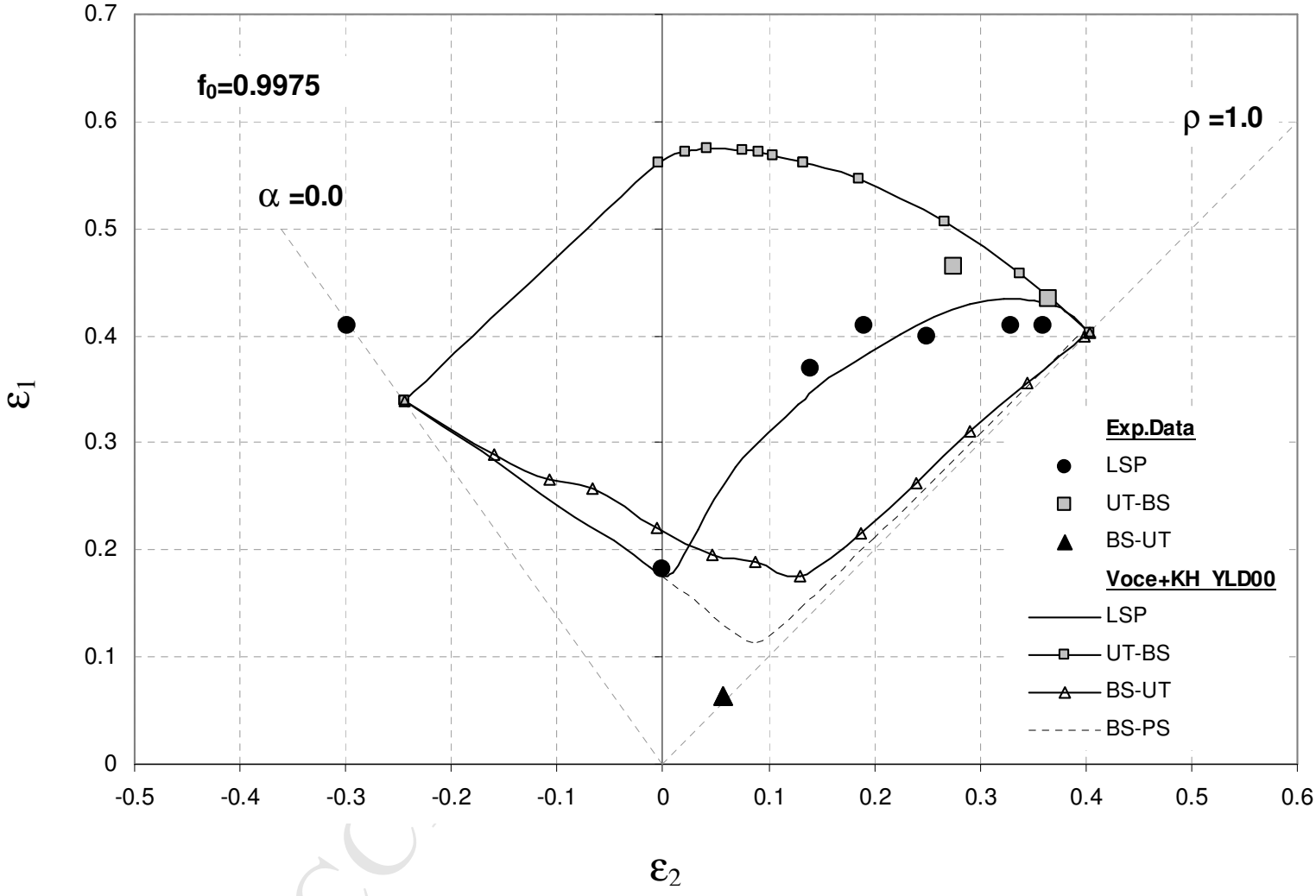

Fig. 7. Experimental and theoretical FLDs under linear and complex strain paths for DC06 steel sheet, using Voce law + kinematic hardening and YLD2000-2d yield function.

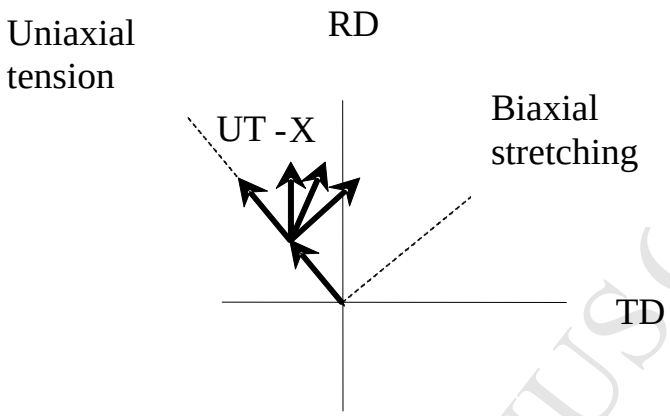

Fig. 8. Representation of complex strain paths UT-X

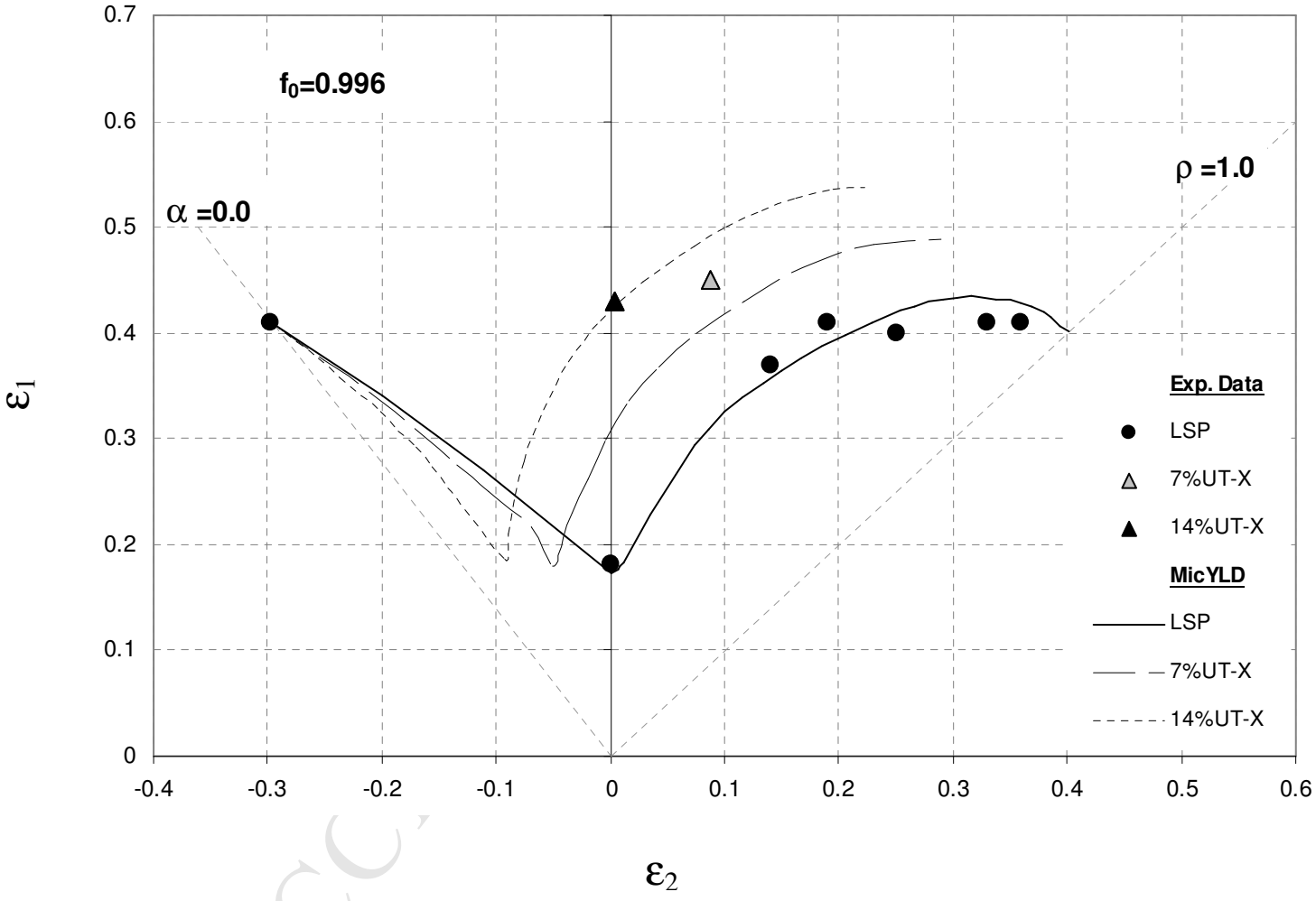

Fig. 9. Experimental and theoretical FLDs under linear and complex strain paths (UT-X) for the DC06 steel sheet, using MicMod and YLD2000-2d yield function.

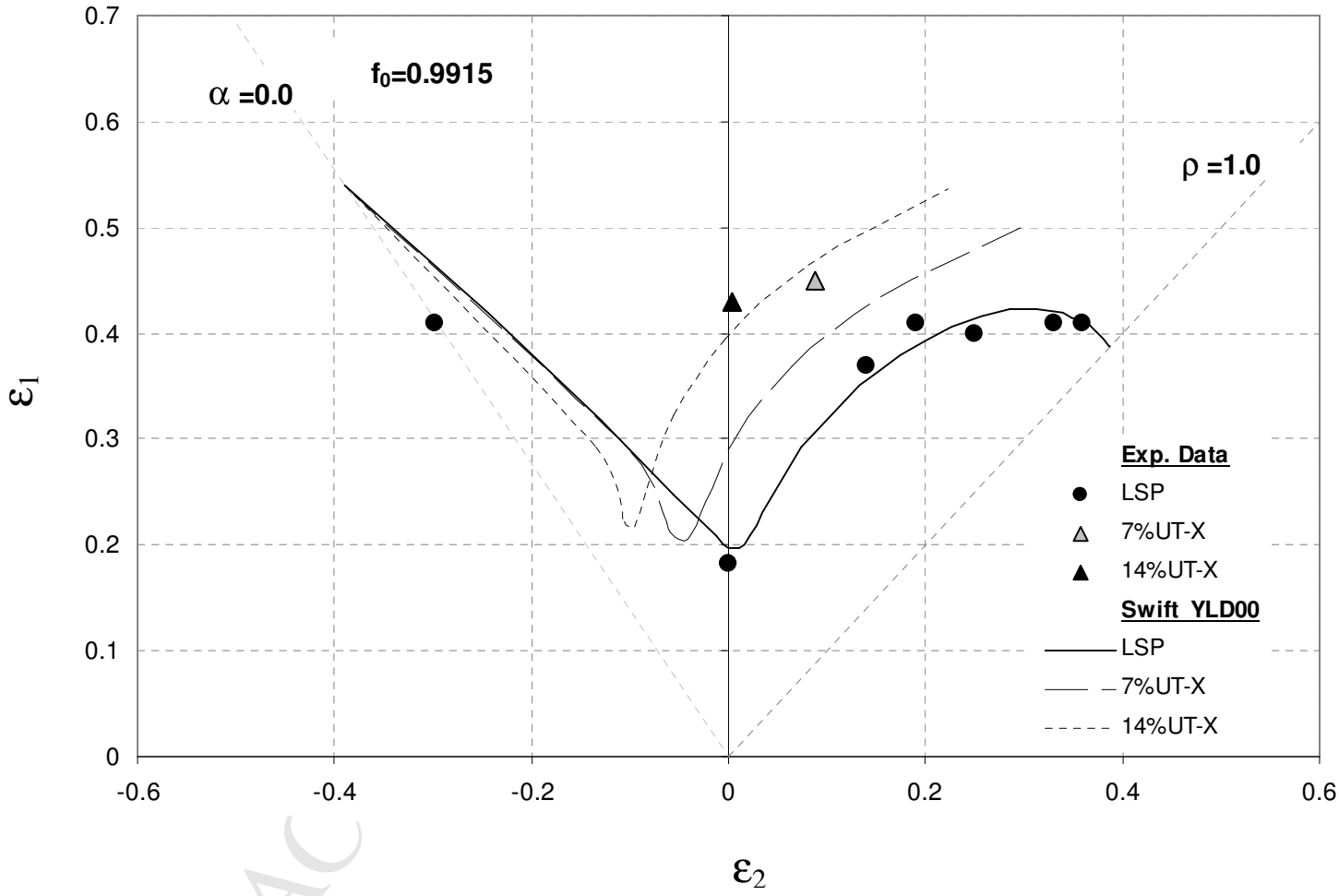

Fig. 10. Experimental and theoretical FLDs under linear and complex strain paths (UT-X) for DC06 steel using Swift law and YLD2000-2d yield function.

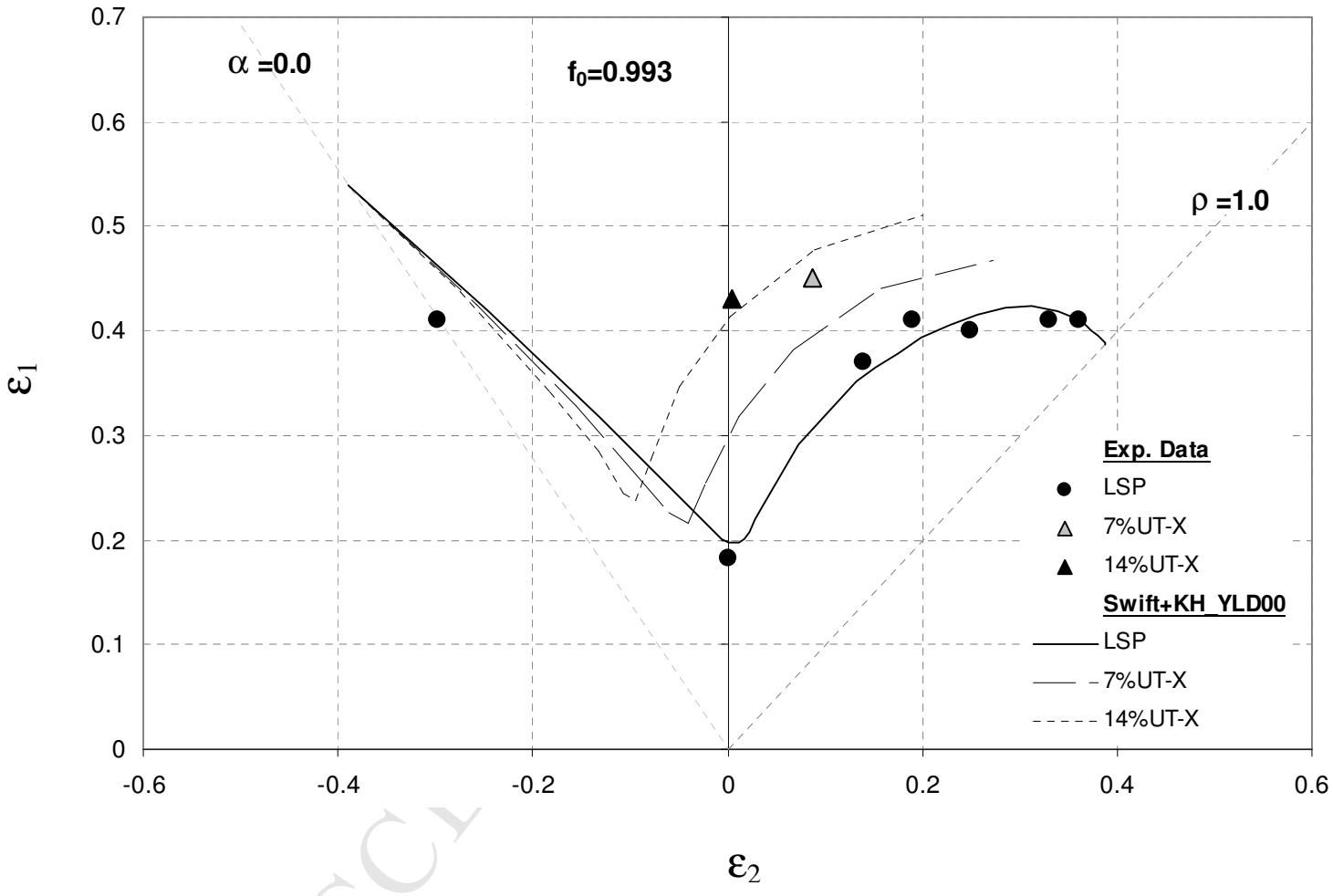

Fig. 11. Experimental and theoretical FLDs under linear and complex strain paths (UT-X) for DC06 steel, using Swift law + kinematic hardening and YLD2000-2d yield function.

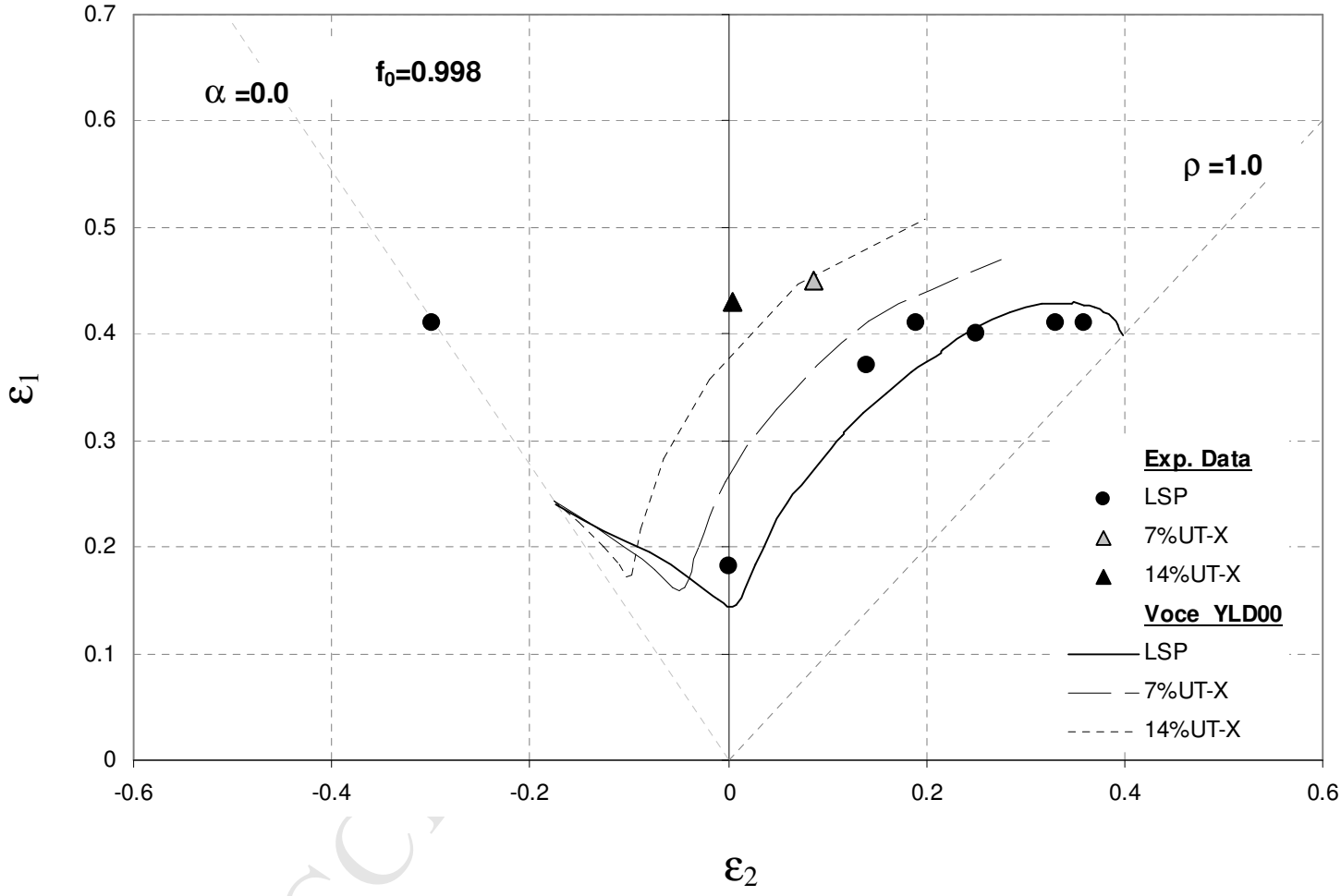

Fig. 12. Experimental and theoretical FLDs under linear and complex strain paths (UT-X) for the DC06 steel, using Voce law and YLD2000-2d yield function

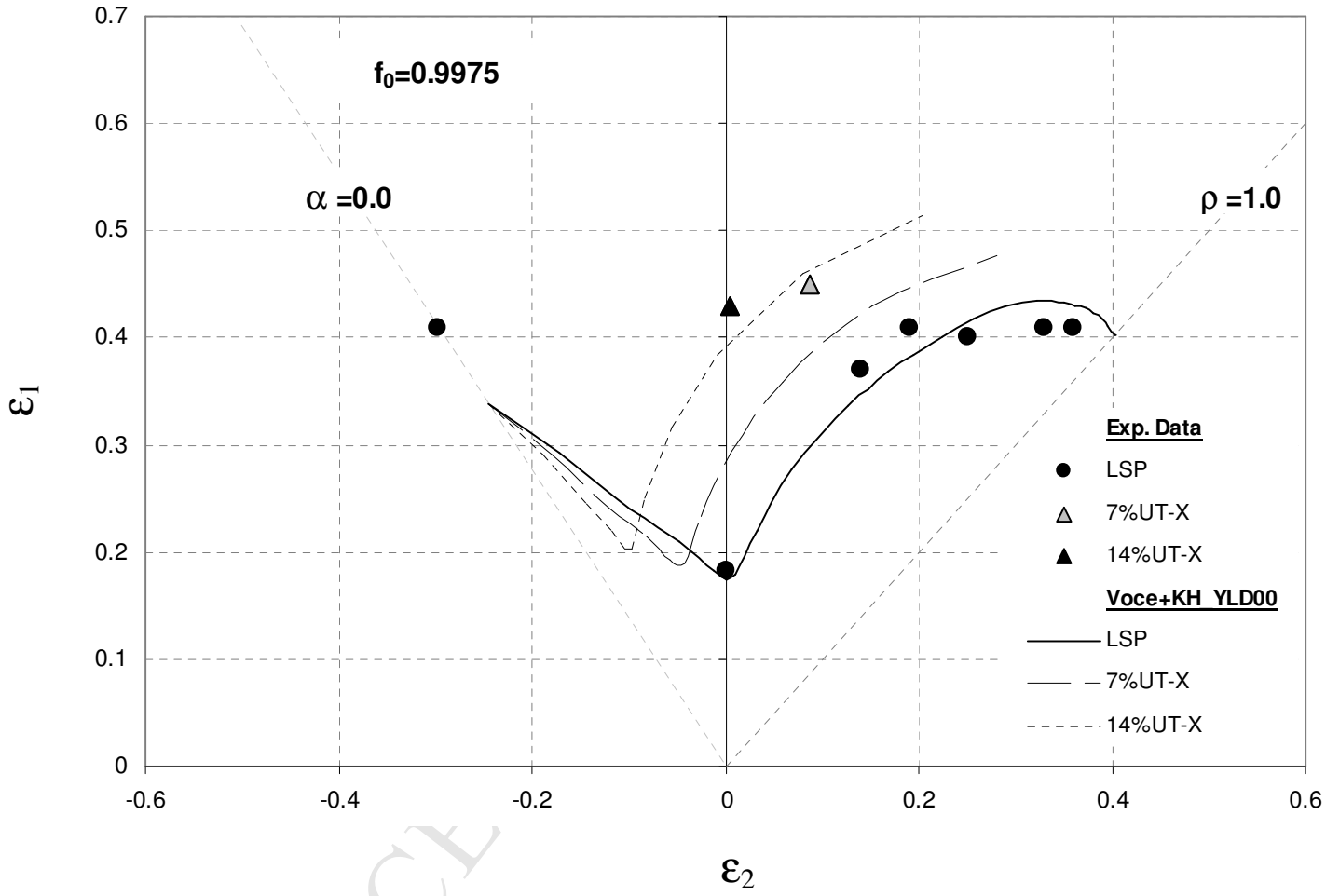

Fig. 13. Experimental and theoretical FLDs under linear and complex strain paths (UT-X) for the DC06 steel using Voce law + kinematic hardening and YLD2000-2d yield function

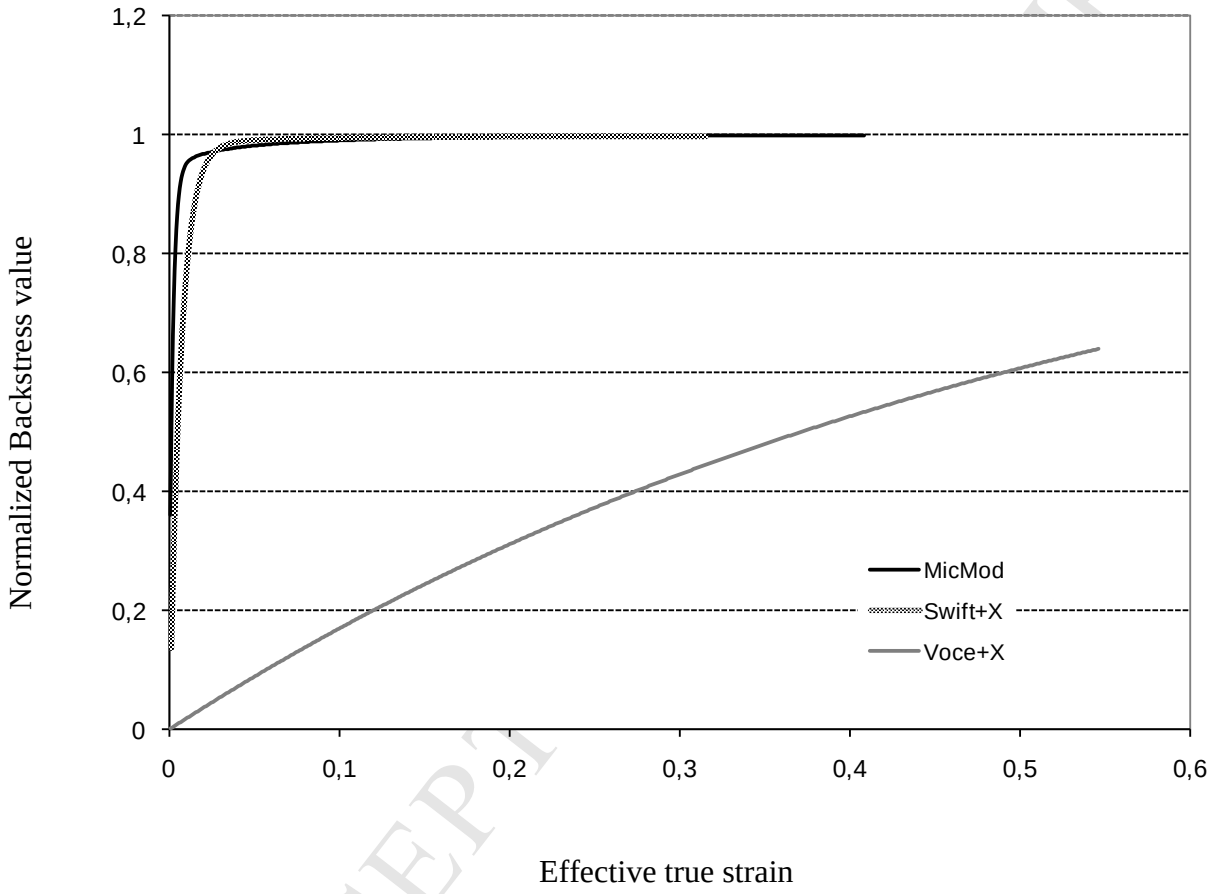

Fig. 14. Evolution of the normalized back stress under uniaxial tension at 0º from RD.

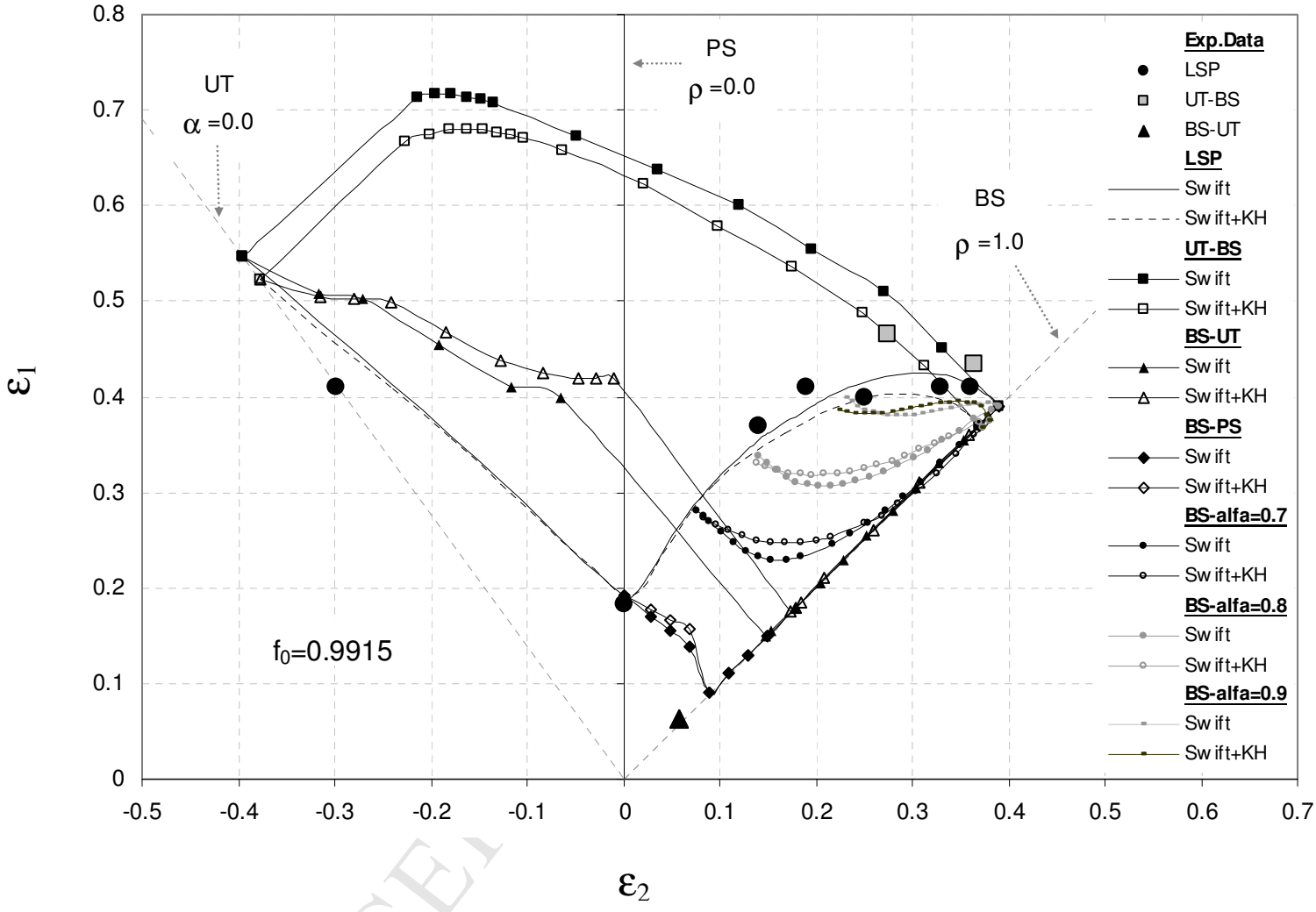

Fig. 15. The influence of the back stress on the predicted FLDs, using Swift law with and without kinematic hardening

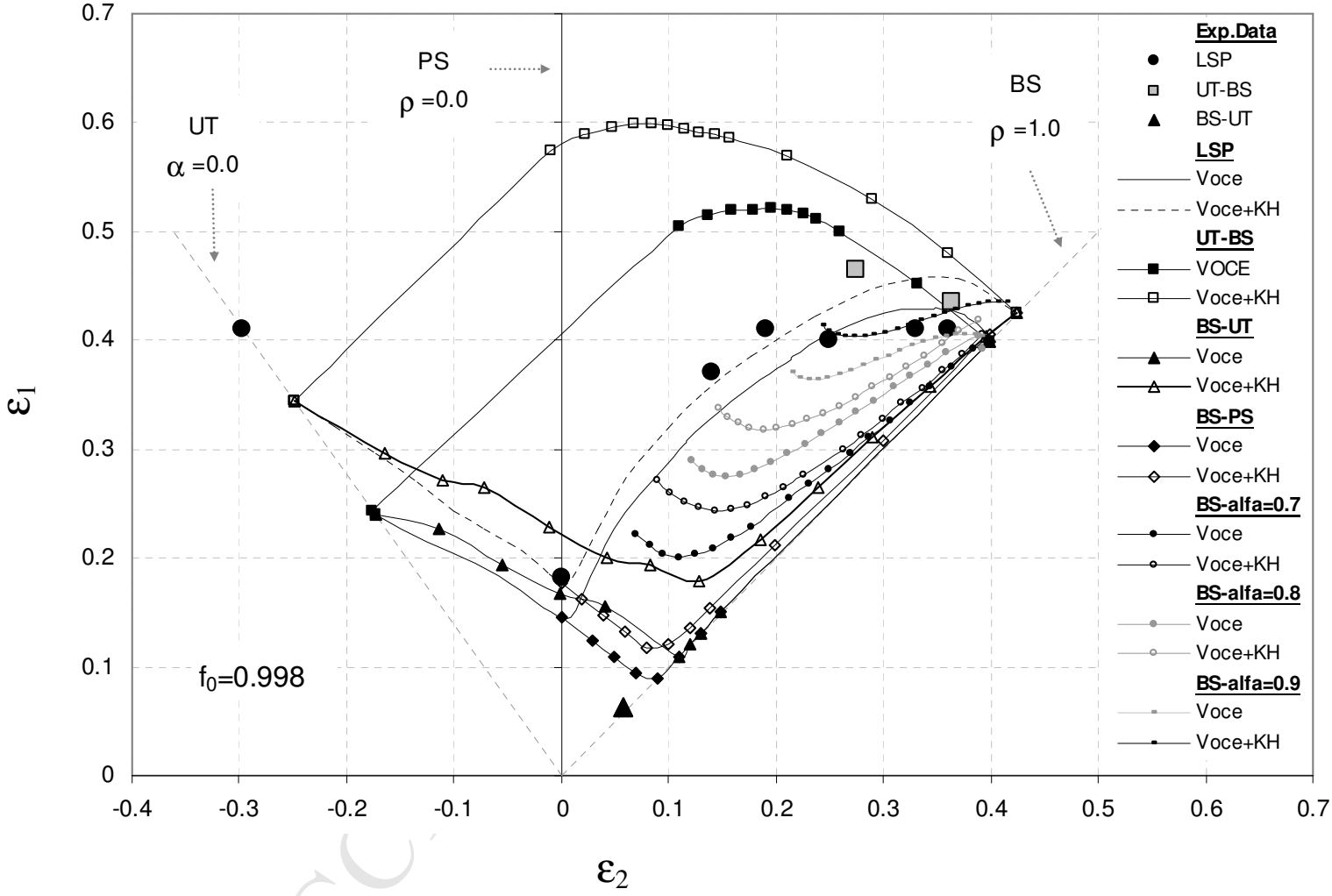

Fig. 16. The influence of the back stress on the predicted FLDs, using Voce law with and without kinematic hardening.